



8-2009

## High Resolution X-ray Tomography of Fiber Reinforced Polymeric Composites

Stephen Andrew Young  
*University of Tennessee - Knoxville*

Follow this and additional works at: [https://trace.tennessee.edu/utk\\_gradthes](https://trace.tennessee.edu/utk_gradthes)

 Part of the [Engineering Science and Materials Commons](#)

---

### Recommended Citation

Young, Stephen Andrew, "High Resolution X-ray Tomography of Fiber Reinforced Polymeric Composites. " Master's Thesis, University of Tennessee, 2009.  
[https://trace.tennessee.edu/utk\\_gradthes/93](https://trace.tennessee.edu/utk_gradthes/93)

This Thesis is brought to you for free and open access by the Graduate School at TRACE: Tennessee Research and Creative Exchange. It has been accepted for inclusion in Masters Theses by an authorized administrator of TRACE: Tennessee Research and Creative Exchange. For more information, please contact [trace@utk.edu](mailto:trace@utk.edu).

To the Graduate Council:

I am submitting herewith a thesis written by Stephen Andrew Young entitled "High Resolution X-ray Tomography of Fiber Reinforced Polymeric Composites." I have examined the final electronic copy of this thesis for form and content and recommend that it be accepted in partial fulfillment of the requirements for the degree of Master of Science, with a major in Engineering Science.

Dayakar Penumadu, Major Professor

We have read this thesis and recommend its acceptance:

Roberto S. Benson, John D. Landes

Accepted for the Council:

Carolyn R. Hodges

Vice Provost and Dean of the Graduate School

(Original signatures are on file with official student records.)

To the Graduate Council:

I am submitting herewith a thesis written by Stephen Andrew Young entitled "High Resolution X-ray Tomography of Fiber Reinforced Polymeric Composites." I have examined the final electronic copy of this thesis for form and content and recommend that it be accepted in partial fulfillment of the requirements for the degree of Master of Science, with a major in Engineering Science.

Dayakar Penumadu

---

Major Professor

We have read this dissertation  
and recommend its acceptance:

Roberto S. Benson

---

John D. Landes

---

Accepted for the Council:

Carolyn R. Hodges

---

Vice Provost and

Dean of the Graduate School

**HIGH RESOLUTION X-RAY TOMOGRAPHY OF FIBER  
REINFORCED POLYMERIC COMPOSITES**

A Thesis  
Presented for the  
Master of Science  
Degree  
The University of Tennessee, Knoxville

Stephen Andrew Young

August 2009

## **DEDICATION**

I dedicate this thesis to my recognition of the Universal Mind, my parents, Dr. John H. Young, Jr. and Sonja Young, and my brothers, John H. Young III, and Paul K. Young, for their unending love, support, and encouragement. Together they have inspired me to live a life with integrity.

## **ACKNOWLEDGEMENTS**

My heartfelt thanks and deepest appreciation go to my advisor, Dr. Dayakar Penumadu, giving me an opportunity and his guidance, patience, and support throughout the course of my study. My wholehearted thanks also go to the distinguished members of the Committee, Dr. Roberto S. Benson and Dr. John Landes for reviewing of this thesis. I would like to express my gratitude to Mr. James T. Pippin for his guidance and support throughout my course of study. In addition I would to express my gratitude to Walter Odom, Dr. Ronald McFadden, Celeste Brooks, Ken Thomas, Douglas E. Fielden, Vlastimil Kunc, Jaret Fratjord, Ashely Stowe and Robin Woracek throughout my course of study. Without their inestimable assistance, this research would not have been possible.

## **ABSTRACT**

A high resolution x-ray tomography system was used to study chopped fiber polymeric composites made of polypropylene resin, nickel coated carbon fiber and E-glass fiber. Procedures are developed to obtain micro-structured features of importance. In-situ tensile testing system was developed and integrated into the existing hardware for tomography equipment to study the evolution of damage and micro-structural features as a function of mechanical stress. High resolution x-ray tomographic images of glass fiber were collected and viewed on a micron scale. The radiographs were reconstructed to visualize the fiber content of the samples in three dimensional volume. In addition, glass fiber dogbone specimens were tested on a miniature tensile machine using x-ray tomography to view deformation of the samples in high resolution. Fractures in the chopped glass composite were observed for x-ray microscopy showing the dominant failure mechanism of the sample are low interfacial strength and adhesion between the fiber and matrix. Cracks were not observed until after failure by fiber pull-out using the digital microscopy method. Using SEM microscopy method, resin cracking and fiber debonding was observed for a carbon fiber with vinyl ester resin while under tensile loading. Important micro-structural information relationship with and mechanical behavior including variation modulus, yield and ultimate strength are discussed.

# TABLE OF CONTENTS

<b>Chapter</b>	<b>Page</b>
<b>1 INTRODUCTION</b>	<b>1</b>
<b>2 HIGH RESOLUTION X-RAY TOMOGRAPHY OF CHOPPED FIBER POLYMERIC COMPOSITES</b>	
2.1 Introduction	3
2.2 Materials and experimental setup	5
2.2.1 Composite Specimens	5
2.2.2 Micro-XCT Experimental Set-up	7
2.2.3 Fiber Volume Fraction	8
2.3 Experimental results	9
2.3.1 Fiber Length Distribution, 3D Reconstruction, and Fiber Volume Fraction	9
2.3.2 Effective Moduli	12
2.4 Conclusion	16
<b>3 IN-SITU DAMAGE EVOLUTION OF POLYMERIC COMPOSITES USING RESOLUTION X-RAY TOMOGRAPHY, DIGITAL MICROSCOPY, AND LARGE CHAMBER SEM</b>	
3.1 Introduction	17
3.2 Materials	21
3.2.1 Composite Specimens	21
3.3 Experimental Procedure and Results	21

3.3.1 Tensile Testing	21
3.3.2 Micro-XCT In-situ Mechanical Testing System	22
3.3.3 In-Situ Mechanical Tensile Testing System using Digital Optical Microscopy	25
3.3.4 In-situ Mechanical Tensile Testing using Large Chamber Scanning Electron Microscope (LC-SEM)	32
3.4 Conclusion	36
<b>REFERENCES</b>	<b>38</b>
<b>APPENDIX</b>	<b>45</b>
<b>VITA</b>	<b>63</b>

## LIST OF FIGURES

<b>Figure</b>		<b>Page</b>
2.1	Schematic of the 3 mm thick pellet injection molding of E-glass fiber/polypropylene ISO-plaque and center-gated disk	46
2.2	Schematic diagram of the skin, shell, and core layers of the E-glass fiber polypropylene molding compound at 50x magnification.	46
2.3	Radiograph of an absorption Radon transform projection of the E-glass fiber with polypropylene matrix at 4x magnification.	47
2.4	Illustration of tomography raw image collection. E-Glass fiber with polypropylene matrix composite sample (0.5 mm x 0.5 mm x 10 mm) inside sample holder. The X-ray source (100 kV, 10 W) and thermoelectrically cooled scintillation CCD detector (2048 x 2048 pixels, 16 bit) at -59 °C with fast readout scintillation crystal.	47
2.5	Radiograph x-ray at 20x, and (b-c) 2D reconstruction slices of the cross section.	48
2.6	8-bit grayscale tomography reconstruction and corresponding thresholded image of E-glass fiber with polypropylene matrix composite sample. Thresholded and measured E-glass fibers in the area of interest.	48
2.7	Fiber Length Distribution of E-glass fibers in polypropylene matrix.	49
2.8	Figure 8: Area Density Distribution for fast-filled and slow-filled E-glass fibers in polypropylene matrix.	49

2.9	3D reconstructed images of the E-glass fiber with polypropylene matrix.	50
2.10	Flow chart to determine effective moduli for the E-glass fiber in polypropylene matrix.	50
2.11	(a) 8-bit grayscale tomography reconstruction, (b) corresponding thresholded image and (c) effective modulus for slow-filled E-glass fiber with polypropylene.	51
2.12	Figure 12: Effective modulus, E-glass spheres in polypropylene matrix.	52
3.1	Schematic of the 3 mm thick, 45° [ $\pm 45$ , 2s] carbon fiber with vinyl ester resin and tensile sample.	53
3.2	Schematic of (a) E-glass fiber/polypropylene dogbone composite sample and (b) corresponding finite element analysis stress concentration distribution.	54
3.3	In-situ mechanical tensile system with actuator and 1334.5 N (300 lbf) load cell. E-Glass fiber with polypropylene matrix composite sample (2.3 mm x 1.4 mm x 55.78 mm) inside sample holder. The X-ray source (100 kV, 10 W) and thermoelectrically cooled scintillation CCD detector (2048 x 2048 pixels, 16 bit) at -59 °C with fast readout scintillation crystal.	54
3.4	Radiograph of transmission Radon transform projection of the E-glass fiber with polypropylene matrix at 4x magnification (a) before tensile loading (b) during tensile loading and (c) after failure of the tensile sample.	55

3.5	Experimental data corresponding to fast-filled E-glass fiber with polypropylene dogbone sample.	55
3.6	(a) 2-D reconstruction of E-glass fiber with polypropylene resin and (b) corresponding 3-D volumetric rendering after tensile loading.	56
3.7	Typical experimental data for a tensile test for E-glass/polypropylene.	57
3.8	Fracture surface of E-glass with polypropylene resin after tensile failure.	57
3.9	Typical experimental data for a tensile test for carbon fiber with vinyl ester resin.	58
3.10	Fracture surface of carbon fiber/vinyl ester after tensile failure for (a,b) by fiber pullout and (c) cleavage fracture.	59
3.11	Experiment setup for the in-situ mechanical system in LC-SEM.	59
3.12	Damage evolution of carbon fiber/vinyl ester tensile sample under tensile loading.	60
3.13	Load-Displacement damage evolution of carbon fiber/vinyl ester tensile sample under tensile loading.	60
3.14	Damage pattern of carbon fiber vinyl ester and (b) fracture surface of carbon fiber/vinyl ester fiber after tensile failure.	61

# CHAPTER 1

## INTRODUCTION

Polymeric composites made of glass or carbon fiber and polypropylene resin have been of significant interest in the automotive field due to their light weight, resistance to corrosion, and high strength. Despite these advantages, the mode of failure of such materials is typically sudden due to failure in fibers, resin, or their combination. In this research, high-resolution tomography was attempted to evaluate the state of micro-structure and damage evolution as function of mechanical stress. High resolution x-ray tomographic images of glass fiber and nickel-coated carbon fiber composites were collected at exceptional resolution with sub-micron scale. The radiographs will be reconstructed to visualize the fiber arrangement of the samples in three dimensional volume. In addition, glass fiber dogbone specimens were tested on a custom miniature tensile machine using x-ray tomography to view deformation of the samples as a function of applied stress.

The microstructure of polymeric composite materials can significantly influence its overall functional properties such as its mechanical strength, electrical and thermal conductivity. Factors including total number of fibers in the matrix, diameter, length, orientation of fibers, interface adhesion with matrix polymer, and pore structure affect the properties. Micro-tomography (Micro-XCT) can produce images with a sufficient resolution to study composites with features including small diameter fibers (e.g. 5 to 15  $\mu\text{m}$ ). Analysis of 2D or 3D can provide an accurate description of microstructure, such as fiber volume ratio, fiber distribution and orientation. The evaluation of micro-structure

under mechanical stress is of interest to develop an understanding of fracture and fatigue behavior of such materials.

A high resolution x-ray tomography system was used for the first time to study chopped fiber polymeric composites made of polypropylene resin, nickel coated carbon fiber and E-glass fiber. The research project evaluated challenges of developing procedures to obtain quantitative micro-structural features of significance. In addition, in-situ tensile testing system was developed and integrated into the existing hardware for tomography equipment to study the evolution of damage and micro-structural features as a function of mechanical stress with ORNL collaboration. This research will pave the way to quantify damage and develop new class of scale-dependent constitutive models for composites materials for immediate use in structural and transportation applications.

## **CHAPTER 2**

### **HIGH RESOLUTION X-RAY TOMOGRAPHY OF CHOPPED FIBER**

#### **POLYMERIC COMPOSITES**

This chapter is a slightly revised version of a paper with the same title submitted for the Journal of Composites Science and Technology in 2009 by Stephen A. Young, Dayakar Penumadu, and Vlastimil Kunc.

My primary contributions to this paper include: (i) development of the problem into a work, (ii) identification of the study areas, (iii) gathering and reviewing of literature, (iv) sampling, processing, and analyzing reconstructed x-ray images from x-ray radiography and tomography, (v) pulling various contributions into a single paper, (v) most of the writing.

#### **Abstract**

Polymeric composites have been of particular interest in the automotive field due to their low weight, high strength, and resistance to environmental degradation. In this research, high resolution x-ray images of chopped glass fiber composites are obtained with a high spatial resolution of 3  $\mu\text{m}$ . The radiographs were reconstructed to visualize the fiber and matrix arrangement in three dimensions with an ability to analyze microstructure including cracks, local fiber volume distribution, fiber morphology after extrusion, and interfacial bonding issues. A simple quantitative approach of using x-ray digital tomographs to obtain spatial variation of composite mechanical properties is demonstrated for the E-glass/polypropylene composite using a composite sphere

analytical model. Important micro-structural information such as the variation of fiber length distribution with distance from the injection molding location is included.

## **2. Introduction**

This paper presents results on using x-ray computed micro-tomography (Micro-XCT) to evaluate the mechanical behavior of short fiber reinforced composites considering its microstructure. Pellet injected E-glass composite fiber specimens with polypropylene resin were evaluated as part of the ongoing research project between University of Tennessee, Oak Ridge National Laboratory (ORNL), Pacific Northwest National Laboratory (PNNL), and Delphi Corporation. The goal of this research is to evaluate and predict the mechanical properties of short fiber reinforced composites in 2D and 3D architecture [1]. Spherical inclusions surrounded by a resin matrix have been used successfully to model the local and global constitutive behavior of the composites [2-3]. This analytical model was implemented by the authors in this study to integrate 3D microstructural measurements from tomography to predict spatially resolved composite mechanical properties. The pellet injection molding process influence on mechanical properties of composites and benefits of chopped fibers are well known [4-6].

Past research has not been performed on evaluating the mechanical properties of E-glass and polypropylene chopped fiber composites considering detailed micro-structure information mainly due to a lack of precise non-destructive measurement technique. Homayonifar [7] has analyzed the matrix-fiber interaction showing that increasing matrix volume fraction causes variation in stress distribution along the fiber length. In the past, automatic image analysis have been successfully used to count and accurately measure

fiber length with straight and curved fibers over large fiber aspect ratios using 2D optical images. However, these techniques require destructive techniques such as burning resin after extrusion to obtain digital images of chopped fibers in a dispersed state [8-9]. X-ray imaging is becoming important non-destructive approach due to its ability to provide a detailed three dimensional visualization of the polymeric composites for subsequent quantitative analysis to obtain fiber structure and orientation [10].

## **2.2 Materials and experimental setup**

### **2.2.1 Composite Specimens**

The composite material used in this study included polypropylene resin having E-glass fibers manufactured by Montsinger Technologies, Inc. using a fiber melt process. The chopped E-glass fiber roving was 12.7 mm in length with a diameter of 17  $\mu\text{m}$  [1]. Detailed manufacturing aspects of the composites were presented elsewhere [1] and a brief explanation is included this paper here.

As shown in Figure 1, in the Appendix, the ISO-plaque and center-gated disk geometries were used for the pellet injection molding using two volumetric flow rates (16.4 and 131.2  $\text{cm}^3/\text{s}$ ) to evaluate effect of the injection speed on the as-formed microstructure of chopped fiber composites and corresponding physical properties. The mold temperature was held at 78  $^{\circ}\text{C}$ , while the inlet temperature of the melt was 240  $^{\circ}\text{C}$ . The center gated disk is 3 mm thick and 177.8 mm in diameter. The ISO-plaque is 3 mm thick, 90 mm long and 80 mm wide. The flow direction for the center gated disk and ISO-plaque was radially outward as illustrated in Figure 2.1b. The bulk density of the E-glass fiber composite with polypropylene resin composite was 1.2203  $\text{g}/\text{cm}^3$  [1]. The

fiber weight fraction corresponded to 40% for E-glass fiber/polypropylene (GF/PP) molding compound which leads to approximately 20% global fiber volume fraction. Figure 2.1 shows three regions (A,B,C) of interest in our study to evaluate fiber length and fiber orientation measurements. The A, B, C regions corresponds to 6, 34, 64 mm distance from the center of the disk and 15, 45, and 75 mm from the injection point of the ISO-plaque sample as denoted in the figure. Typical crystallinity values of ISO-plaque molding compounds for the A, B, C regions were observed to be 47.6 %, 45.5 %, and 43.5%.

The morphology of fibers and mechanical properties of the composite samples were studied using x-ray imaging to view the chopped fibers composites at 3 microns resolution. As shown in Figure 2.2, cubical samples having a size of 2 mm x 2 mm x 10 mm (with the fibers in the transverse direction) were obtained from the specified A, B, and C region using a diamond saw. Figure 2.2 displays surface image from an optical micrograph showing the skin, shell and core layer structure of the GF/PP sample. The velocity at the core is higher than the shell and skin layer due to the velocity profile of the melt in contact with the wall inside the injection molding machine. Prior research found that the higher velocity gradient in the core layer results increased fiber orientation and improved mechanical properties in the direction of flow [11]. One edge normal to the transverse fibers was polished for optical microscopic observations where photomicrographs were taken to analyze the fiber length and orientation measurements.

### 2.2.2 Micro-XCT Experimental Setup

The use of Micro-XCT provides the benefit of fiber characterization in a nondestructive manner. The computed tomography used in our research affords high resolution (3  $\mu\text{m}$ ) to view the spatial variation of the x-ray absorption for various projection views. X-ray absorption depends on several factors including density, length of absorbing material transversed by beam, and the x-ray wavelength [10]. The principles of x-ray imaging and computed tomography are covered in detail by Stock, Kak and Slaney, and Banhart [12-14].

The transmission intensity through a sample is governed by the Beer-Lambert Law shown in Eq. 1.

$$I(x, y) = I_0(x, y)e^{\int_0^s -\mu(x, y) \cdot ds} \quad (2.1)$$

where  $I_0$  is the incident intensity of the x-ray beam before passing through the a distance  $ds$  of the sample with attenuation coefficient  $\mu(x, y)$ . For composite samples, an average value of  $\mu(x, y)$  can be calculated from the weight fraction of each element and mass

absorption coefficient,  $\frac{\mu}{\rho}$  [12]. The attenuation is measured along the x-ray paths using

$\mu(x, y)$ , to generate 2D projections. For each tomography experiment, 2D radiographs

[Figure 2.3] are taken at many different angular positions. This results in a set of

projections that are used for reconstructing a complete 3D image representing local

attenuation of the sample. Mathematically, this corresponds to inverting the Radon

transform of the projection data. To achieve this, a filtered back projection algorithm was

used. The number of projections has to be sufficiently high to obtain good spatial resolution of reconstructed image which depends on x-ray optics, scintillator, exposure time, and sample type. Ring artifacts are reduced by using flat-field corrected images.

The MicroXCT series x-ray transmission 3D tomographic microscope developed by Xradia, Inc. ([www.xradia.com](http://www.xradia.com)) was used in this research as shown in Figure 2.4. The MicroXCT is a transmission-type full field imaging x-ray microscope. The sample tower allows translations in x,y,z directions and rotation ( $\theta$ ) up to  $175^\circ$ . The maximum sample size this testing system accommodates is a cube of 75 mm and rotation stage limits samples having weight less than 4.5 kg (9.9 lbs).

In this research, the x-ray source was positioned at 40 mm from the rotational axis and a thermoelectrically cooled scintillation CCD detector was used 20 mm from the rotational axis. Two magnifications of 4x and 20x with a field of view of 5 mm x 5 mm and 1 mm x 1 mm were used in the present study.

As illustrated in Figure 2.4, the x-ray images data were acquired by MicroXCT X-ray beam penetrating the sample on a rotating sample stage. High resolution was obtained by maximizing the geometric magnification of the object on the detector with reduced blur [10]. The flat-field corrected tomographic raw images were reconstructed using grayscale 8-bit image at 1x and 4x binning with the absorption values ranging from 0 to 255.

### 2.2.3 Fiber Volume Fraction

The areal method, where the number of black and white pixels (after suitable thresholding) within the specified region of interest (representing the matrix and fiber,

respectively) were counted using a computational algorithm to determine the fiber volume fraction by integrating the information from a stack of images. Since the area associated with each pixel is equal, the fraction of the total pixels for each constituent material becomes the fraction for that constituent [15]. Two image processing programs, ImageJ and Image-Pro Plus, were used for analysis for the reconstructed slices of the composite samples. ImageJ image processing program was used to create an .avi file of the reconstructed slices. ImagePro Plus® was used to calculate volume fraction of the fiber content using series of reconstructed slices of the GF/PP sample.

The rule of mixtures was used to determine the fiber volume fraction for each binary reconstructed slice:

$$c = \frac{V_i}{V_i + V_m} * 100\% \quad (2.2)$$

where  $V_i$  = volume fraction of fiber content

$V_m$  = volume fraction of polymer matrix

$V_f$  = volume fraction percentage of fiber to polymer matrix

## 2.3 Experimental results

### 2.3.1 Fiber Length Distribution, 3D Reconstruction, and Fiber Volume Fraction

Figure 2.5a shows a typical radiograph taken at a magnification of 20x for the slow-filled GF/PP composite sample with 0.92 mm field of view taken at 1x binning. It is a transmission radiograph for a sample with a size of 0.5 mm x 0.5 mm x 0.8mm obtained from the core layer of the sample. The high contrast between the individual fibers can be seen in this radiograph. Figures 2.5b and 2.5c displays 2D reconstructed slices beneath the surface of the sample where the individual fibers clearly show the

orientation and the geometric arrangement of chopped fibers from the polish side through the thickness of the sample. The high concentration of fiber bundles shown in Figure 2.5b indicates high strength properties for the GF/PP sample. As shown in Figure 2.5b, some ring artifacts from reconstruction can also be seen despite the use of filtering during reconstruction. The elliptical features in Figures 2.5b and 2.5c indicate the fibers are found to be curved in and out the x-y plane view potentially highly stressed, and may be initiation sites for fracture resulting from conditions used in the injection molding process corresponding to the slow-fill rate.

Figure 2.6a shows a typical 2D reconstructed slice of a fast-filled GF/PP sample with high concentration of fibers in the cross section. GF/PP 2D reconstructed slices with a 2 mm x 2 mm view area were thresholded and filtered using custom algorithm implemented in Image-Pro Plus ® imaging software an example shown in Figure 2.6b. In this process, gray scale images of fibers and resin are transferred to binary for quantitative image analysis. Figure 2.6b shows that reasonable representation of gray scale images were obtained with automated threshold value of intensity to obtain binary images. Subsequently, using these binary images, fibers were counted and analyzed as shown in Figs 6b and 6c. Figure 2.7 shows the fiber length distribution (FLD), obtained from twenty slices, for the fast filled GF/PP ISO-plaque composite sample at location A, which appear to favor a shorter length resulting from the plastication process in injection molding probably due to fiber-matrix and fiber-fiber contact, where the brittle behavior of E-glass fiber are prone to breakage [16]. Most fibers are less than 4 mm in length, indicating that the process conditions associated with fast filled volumetric rates have a

high impact on the degradation of fiber length. The mean average fiber length was 0.9 mm, significantly less than the typical critical length value of 1.8 mm for GF/PP [4]. However this is consistent with prior research [17] that as the fiber volume content of short glass fibers increases the mean length decreases. The normalized weight was determined by measuring the relative weight of the measured fiber as a fraction of the original pellet length. The fiber lengths were counted in a length range (e.g. 4-5 mm). Using a nominal pellet length of 12 mm and 4.5 mm long fiber would place  $4.5/12 = 0.38$  in the 4-5 mm length range [6]. The fiber count in the region of interest typically yielded 170 to 300 fibers from a single reconstructed slice.

Figure 2.8 displays the fiber area fraction variation for a fast-filled GF/PP sample (2 mm x 2mm x 3mm). An area of interest (700 pixels by 700 pixels) similar to Figure 2.6b was selected for 700 reconstructed slices to simulate a volume element size of 700 x 700 x 700 voxels to calculate the volume fraction of the GF/PP sample. Using a custom developed image processing algorithm the analysis of the reconstructed slices for this sample, the fiber area percentage was found to vary from 40% to 47%. The slow-filled GF/PP was similarly analyzed and showed a much higher variation of fiber volume fraction from 35% to 59%.

Figures 2.9a and 2.9b show a three dimensional reconstruction cross section of a slow filled GF/PP ISO-plaque composite sample at location C that has been converted to a binary image for quantitative analysis. Beneath the surface, the fibers can be seen lumped together indicating potentially high stress concentrations if this sample were to be subjected to external mechanical loading. The high concentration of fibers locally is

expected to increase the modulus/strength of the material and resulting stress concentrations in that region. The broken fiber ends indicate areas of a weaker surrounding matrix and that debonding will occur under tensile load [18]. Our future planned experiments to view fracture of individual E-glass fibers and matrix under tensile loading using in-situ x-ray imaging approach should confirm such hypothesis and could prove to be very useful for developing suitable process-property relationship for chopped fiber composites. At present time, very small cracks (smaller than 3  $\mu\text{m}$ ) in the fibers and matrix can not be located due to limitation of geometric magnification of 20x.

### 2.3.2 Effective Moduli

Hashin and Christensen [2-3] proposed a simple mathematical model which uses composite sphere analogy to determine the effective properties of composites with binary phases (resin and fiber). The most effective way to utilize such a model has been to average microscale effects and characteristics to predict macroscopic behavior [19]. A representative volume element comprises of a spherical inclusion surrounded by a matrix phase which is ultimately encompassed by an equivalent homogenous medium. This model has been reported to provide reasonably good predicative results for modeling the mechanical properties of fiber reinforced composites [3]. In our research, by selecting a voxel inside the 3D reconstructed sample of the composite, the localized constituent properties now can be analyzed using an analytical model, such as the one proposed by Hashin. In this study, we used the spatial distribution of the 3-phase model that uses fiber volume fraction to determine effective bulk and shear modulus for a given number of voxels.

There are several advantages to using the 3-phase model as outlined by Christensen including a highly localized interfacial shear stress and bulk modulus determination [3]. The model covers the entire volume fraction range in the sense that the spherical inclusions can exist at any level,  $0 \leq c \leq 1$ . A very close prediction of experimentally measured effective uni-axial modulus up to a 50% volume fraction of inclusions ( $c = 0.5$ ) was demonstrated by Christensen [3] for E-glass microspheres in a polyester matrix. The effective bulk modulus,  $k$ , was determined based on a non-dilute elastic suspension of spherical particles. The bulk modulus has a displacement condition imposed on a single composite sphere with upper and lower bounds. Hence, the spherical inclusion is treated as a displacement field in a representative volume element based on the theorem of minimal potential energy. This procedure will allow calculating the localized bulk modulus in the volume element. The bulk modulus is derived as shown in Eq. 3, where  $k_i$  and  $k_m$  are the inclusion and matrix bulk moduli respectively,  $\mu_m$  is the shear modulus of the matrix, and  $c$  is the volume fraction of inclusions [3].

$$k = k_m + \frac{c(k_i - k_m)}{1 + (1 - c) \left[ (k_i - k_m) / \left( k_m + \frac{4}{3} \mu_m \right) \right]} \quad (2.3)$$

As shown in Eq. 4, the effective shear modulus of composite material is obtained from the positive root where parameters  $A$ ,  $B$ , and  $C$  are defined in the Appendix (See A.1).

$$A \left( \frac{\mu}{\mu_m} \right)^2 + 2B \left( \frac{\mu}{\mu_m} \right) + C = 0 \quad (2.4)$$

The purpose of Eq. 4 is to calculate the effective shear modulus since the inclusion is composed of two materials and does not experience a uniform stress state. [3]. The three phases of the model is the fiber (inclusion), fiber interface with the resin matrix, and the surrounding resin representing the homogeneous medium.

Figure 2.10 illustrates the process of selecting a representative volume element from a three dimensional reconstruction, the above describe method of using 2D reconstructed slices was implemented. Several local volumetric elements from x-ray tomography reconstruction images were selected from two GF/PP composite samples at different fill rates to determine the fiber volume fraction variation. As shown in Eq. 5, for each volume element, the mechanical properties were determined in finding the effective bulk, shear, and Young's modulus,  $\frac{E}{E_m}$ , where

$$E = \frac{9k\mu}{3k + \mu} \quad (2.5)$$

Figures 2.11a and 2.11b show a grayscale reconstruction image of the slow-filled GF/PP sample having a cross section of 0.5 mm x 0.8 mm thresholded using the Amira 3.0 volume visualization imaging software. Figure 2.11c shows the variation of  $c$  and the corresponding effective Young's modulus of the selected volume elements in Figure 2.11b. Areas of interest similar to the images shown in Figures 2.11a and 2.11b with the voxel size of 100 x 100 x 74 were used to calculate the fiber volume fraction representing the volume element. Figure 2.12 shows the volume fraction variation and effective modulus for E-glass chopped fibers embedded in polypropylene matrix for two fill rates for eight areas of interest. The fast filled GF/PP composite sample is located in location

A on the ISO-plaque as shown in Figure 2.1a. This sample had a fiber volume fraction range of  $0.39 \leq c \leq 0.46$  and an effective modulus range of  $4.0 \leq \frac{E}{E_m} \leq 4.5$ . The slow-filled GF/PP composite sample is located in location C on the center-gated disk shown in Figure 2.1b. The fiber volume fraction ranges were  $0.35 \leq c \leq 0.63$  and effective modulus range of  $3.4 \leq \frac{E}{E_m} \leq 7.9$ . The fast filled sample had a small fiber volume fraction and strength variation between fiber and matrix through the thickness of the sample. The slow-filled composite has a wider range of fiber volume fraction variation and effective modulus indication stronger and weaker interface between fiber and matrix through the thickness of the sample. A Poisson ratio value of 0.21 was assumed for E-glass spherical inclusion and 0.32 for polypropylene matrix [20]. The results shown in Figure 2.12 indicate that the elastic modulus increased with fiber content for both fast-filled and slow-filled samples. Based on the results, additional factors such as yield stress and fracture toughness are known to increase with glass fiber content [18]. In addition, the strain to failure will decrease with increased amount of fibers, although the increased brittle behavior of the composite is due to a higher amount of E-glass fiber content [16].

Using a 3-phase analytical model, the effect of the fiber volume fraction is related to an increase in mechanical properties as shown in Figure 2.12. The advantage this model allows the study of the microstructure of the composite for local areas of interest, providing a good prediction of mechanical properties including the effective shear and elastic modulus based on fiber volume fraction,  $c$ .

## 2.4 Conclusion

A novel experimental technique was developed to evaluate the microstructure of chopped fiber polymeric composites, made of polypropylene resin with E-glass fiber using a high resolution x-ray tomography system. A method was implemented to characterize the microstructure quantitatively using fiber volume fraction from three dimensional x-ray images. Using a three phase analytical model and spatially resolved microstructural features, spatial variation of elastic modulus composite samples are predicted. Using x-ray tomography, actual variation of fiber volume fraction for local regions of interest from the bulk composite specimen were measured along with spatial variation of moduli. The effect of the fiber volume fraction is directly related to mechanical properties. The slow filled GF/PP had a higher fiber volume fraction variation than fast-filled. This research demonstrates the use of high resolution in nondestructive techniques to evaluate mechanical properties as a function of composite materials microstructure. In the future, scale-dependent constitutive models for composites materials from such measured data is expected to provide important insight into optimal process conditions and final properties of chopped fiber polymeric composites.

## **CHAPTER 3**

### **IN-SITU DAMAGE EVOLUTION OF POLYMERIC COMPOSITES USING HIGH RESOLUTION X-RAY TOMOGRAPHY, DIGITAL MICROSCOPY, AND LARGE CHAMER SEM**

This chapter is a slightly different version of a paper with the same title that will be submitted for the Journal of Composites Science and Technology in 2009 by Stephen A. Young, Robin Woracek, Dayakar Penumadu, Jaret Frafjord, Ashley Stowe, and Vlastimil Kunc.

My primary contributions to this paper include: (i) development of the problem into a work, (ii) identification of the study areas, (iii) gathering and reviewing of literature, (iv) sampling, processing, and analyzing reconstructed x-ray images from x-ray radiography, digital microscopy and scanning electron microscopy, (v) pulling various contributions into a single paper, (vi) most of the writing.

#### **Abstract**

Polymeric composites have been of particular interest in the automotive field due to their low weight, high strength, and resistance to environmental degradation. In this research, high resolution x-ray images of chopped glass fiber tensile composites are obtained with a high spatial resolution of 3  $\mu\text{m}$  using a unique in-situ tensile testing system. The radiographs were reconstructed to visualize the damage evolution as a function of applied on the composite material in three dimensions with an ability to

analyze microstructure including cracks, fiber morphology, and interfacial bonding. In-situ tensile testing of chopped glass fiber and continuous carbon fiber are evaluated using a chamber SEM microscopy at magnification not possible using x-ray microscopy to study microstructure in great detail. Fractures in the chopped glass composite were observed for x-ray microscopy showing the dominant failure mechanism of the sample is low interfacial strength and adhesion between the fiber and matrix. Cracks were not observed until after failure by fiber pull-out using the digital microscopy method. Using SEM microscopy method, resin cracking and fiber debonding was observed for a carbon fiber with vinyl ester resin while under tensile loading. Important micro-structural information relationship with and mechanical behavior including variation modulus, yield and ultimate strength are discussed.

### **3.1 Introduction**

The Part 1 of the present work [23] dealt with development of a novel technique to evaluate the microstructure of chopped polymeric using x-ray computed micro-tomography (Micro-XCT) and determine the spatial resolved mechanical properties of the composite. A three phase analytical model and microstructural spatially resolved micromechanical features were evaluated as a function of the fiber volume fraction to predict the mechanical properties of the composite. In this study, a unique in-situ tensile testing system, developed by the authors, integrated 3D microstructural measurements from tomography to evaluate spatially resolved composite mechanical properties.

Past research has not been performed on evaluating in-situ deformation and damage behavior of E-glass and polypropylene chopped fiber composites considering

detailed micro-structure information mainly due to a lack of precise non-destructive measurement technique. Tensile fractography analysis has indicated the tensile fractures in the composites are dominated by interfacial failure [24]. Lindhagen and Bergund [25] found using in-situ microscopy of glass fiber that cracks in the composite specimen result from high areas of stress concentration and major damage points of initiation were transversely oriented fibers and fiber bundles. In-situ SEM microscopy has shown in good detail the interfacial adhesion of the polymer matrix onto the fiber. Using electron microscopy methods such as low voltage, high resolution scanning electron microscopy (LV-SEM) has shown different microstructural behavior of polypropylene composites tend to have more brittle behavior which may be accounted for in terms of the time-dependence of damage development [26]. Polarized light microscopy has been used to observed damage zones of E-glass and polypropylene to successfully examine failure mechanisms such as crack propagation [27]. Digital video microscopy mechanical testing has given access the plastic response of polymers under uniaxial tension performed locally at the center of the neck for dogbone polymeric materials [28]. Although digital microscopy and SEM methods have been used to visualize the surface of the polymeric composites surfaces to study the deformation of glass fiber composites, these techniques require destructive techniques deforming the sample to failure state of strain in order to obtain digital images of the fibers beneath the composite surface [25, 27].

MicroXCT imaging is becoming an important non-destructive approach due to its ability to provide a detailed three dimensional visualization of the polymeric composites

for subsequent quantitative analysis to obtain fiber structure and orientation [29]. Micro-XCT has been used to obtain direct observation and measurement of fiber length, width, and volume distribution for fiber-reinforced polymeric composite however in-situ tensile testing has not been used. [30]. X-ray scattering and optical microscopy has been used to study the deformation mechanism for polypropylene where the deformation behavior is thought to depend on crystal phase, spherulite size and lamellar arrangement [31]. In addition, x-ray scattering using stretch hold techniques have been unsuccessfully able to observe micro-features such as stress relaxation [32].

There is a growing interest in carbon fiber with vinyl ester resin (CFVE), a continuous fiber polymeric composite, due to its superior mechanical properties for naval applications, relative ease of fabrication using VARTM technique, and its resistance to environmental degradation. The microstructure of CFVE were also evaluated in this research as part of the ongoing research sponsored by the United States Office of Naval Research (ONR). Shivakumar has predicted elastic behavior based on the simple micromechanical equations of the CFVE composites with experimental data validation with good agreement [33]. In-situ observations of carbon fiber composite specimens using SEM has shown successfully the onset of failure showing that the interfacial failure is the dominant failure mechanism for this material [34]. In our study, a vacuum-suitable mechanical testing system was fabricated to perform unique in-situ studies on polymeric continuous composite samples using high resolution x-ray imaging digital microscopy and large chamber scanning electron microscope (LC-SEM).

## **3.2 Materials**

### **3.2.1 Composite Specimens**

The materials and processing of the pellet injection molded polypropylene resin having chopped E-glass fiber (GFPP) are described in Part 1 [23]. The CFVE composite specimen was made of carbon stitch bonded fabric designated by LT650-C10-R2VE supplied by the Devold AMT AS, Sweden. This was an equibiaxial fabric produced using Toray's Toraya T700 12K carbon fiber tow with vinyl ester compatible sizing. The T700 fiber had a tensile strength at 4.9 GPa, a tensile modulus of 230 GPa and elongation of 2.1%. The matrix used a Dow Chemical DERA KANE 510A-40, a brominated vinyl ester, resin and composite material was fabricated using the VARTM process. The fiber volume fraction was found to be 58% by the area density method and includes 2.2% weight of polyester stitch [33]. The dogbone samples were cut from 45° oriented CFVE material and machined to form the sample as shown in Figure 3.1.

## **3.3 Experimental Procedure and Results**

### **3.3.1 Tensile Testing**

The composite dogbone samples were loaded according to three unique experimental set ups discussed later in this paper. Loading was introduced by means of custom developed in-situ mechanical testing systems under displacement control where loads were monotonically increased until failure. Digital images were captured using a large depth of focus digital microscope in an attempt to observe cracking in gage length section the sample while under tensile loading. The load, displacement, and strain data were continuously recorded until the sample failed. The Young's modulus was

determined from the linear part of stress-strain curve and the yield strength was determined using a 0.2% offset method. Fig 3.2a and Figure 3.2b show a typical dogbone composite sample and corresponding predicated stress concentration distribution of the sample under uniaxial tensile loading using ABAQUS Finite Element Analysis. As shown in Figure 3.2b, the stress concentration is greatest at the center of the neck of the dogbone composite sample.

### 3.3.2 Micro-XCT In-situ Mechanical Testing System

The benefits of the use of Micro-XCT for fiber characterization in a nondestructive manner are described in Part 1 [23]. The MicroXCT series x-ray transmission 3D tomographic microscope developed by Xradia, Inc. ([www.xradia.com](http://www.xradia.com)) and mechanical tensile testing system was used in this research as shown in Figure 3.3. The sample tower with in-situ tensile system allows translations in x,y,z directions and rotation ( $\theta$ ) up to  $160^\circ$ . In this research, the x-ray source was positioned at 40 mm from the rotational axis and a thermoelectrically cooled scintillation CCD detector was used 20 mm from the rotational axis. A magnification of 4x with a field of view of 5 mm x 5 mm were used in the present study. As illustrated in Figure 3.3, the x-ray images data were acquired by MicroXCT X-ray beam penetrating the sample on a rotating sample stage. The flat-field corrected tomographic raw images were reconstructed using grayscale 8-bit image at 1x binning with the absorption values ranging from 0 to 255.

Two fast-filled GFPP samples were loaded using the in-situ mechanical tensile system experimental set up with actuator and 1334.5 N (300 lb-f) load cell shown in Figure 3.3, where two tensile loading techniques were implemented for the GFPP

samples. For the AF3D-1 sample, radiographs similar to Figure 3.4a were taken at 5 seconds exposure time, under displacement control in 22.2 N (5 lb-f) increments, while under tensile loading until the sample failed. For the AF3D-2 sample, radiographs were taken continuously while under tensile loading until a crack initiation site was observed similar to as shown in Figure 3.4b. The sample was then held at a constant displacement to collect tomography projections of the AF3D-2 sample taken on the Xradia system using 1000 projections in a 160 degree view angle over a period of time of three hours. Tomographic images were reconstructed using TXM Reconstructor software to reduce data from raw images to sinograms to reconstructed images using a parallel beam algorithm, to view the fiber morphology of the tensile sample beneath the surface. The reconstructed images were analyzed using Kitware Volview. Following tomography collection the sample was loaded to failure.

In Figure 3.5 it can be seen that the state of stress corresponding to failure (load to cause failure) is substantially different between the tensile samples for the tensile testing techniques discussed above. Figure 3.5 also shows small changes in the initial stiffness (slope of the stress-strain curve) corresponding to the reported tensile Young's modulus (Table 1) for the two loading techniques applied, indicating loading rate on the interpreted modulus was minimal. Strain to failure decreased significantly with the use of the tomography indicating a brittle character and weakening of the matrix. For all practical purposes, these data are expected to deviate significantly from macroscopic stress-strain behavior of GFPP from the techniques used for the x-ray tomography testing due to the effects of stress relaxation in the composite samples.

Relaxation is expected for these materials and holding the displacement constant for a period of time prior to unloading allows for dissipation of relaxation displacements. From Figure 3.5 it can be shown using the above described loading techniques that stress relaxation significantly changes the microstructure substantially weakening fiber and matrix interface. Sample AF3D-1 experienced shorter relaxation periods than AF3D-2, however the stress-strain curve clearly shows the decrease in strength due to the radiographs where sample AF3D-2 decreased 37%, significantly weakening the microstructure of the sample during the tomography collection. This stress relaxation behavior suggests that shear stress in the matrix near the fiber breaks relax, having distribution effect stress profiles in neighboring fibers. This damage accumulation would in a general sense be similar to that of debonding [35].

Figure 3.4a shows a typical transmission radiograph taken at a magnification of 4x for the fast-filled GFPP composite sample with 4.69 mm field of view. Figure 3.4b and Figure 3.4c show the radiograph of the sample during loading and after failure. The high contrast between the individual fibers can be seen in these radiographs indicating a large concentration of fibers in the sample. Although noticeable fracture in the sample could be observed during the loading as shown in Figure 3.4b, very small cracks (smaller than 3  $\mu\text{m}$ ) in the fibers and matrix can not be located due to limitation of geometric magnification of 4x. However, by rotating the stage the failure of the sample can be clearly observed as shown in Figure 3.4c. The failed sample in Figure 3.4c shows typical GFPP composite fiber pull-out behavior, evidenced by a high concentration of exposed broken fibers indicating the glass fibers were perpendicular to the composite during

loading. In addition, bent fibers also shown indicate a decrease in fracture resistance in the GFPP composite sample [36].

Fig 6a displays a typical 2D reconstructed slice beneath the surface of the sample where the individual fibers clearly show the orientation and the geometric arrangement of chopped fibers through the thickness of the sample. The high concentration of fiber bundles shown in Figure 3.6b indicates crack initiation sites for the sample [25]. As shown in Fig 6b, 3D reconstructed fibers of the GFPP can be observed yet the contrast between the fiber and matrix was not great enough to threshold the image accurately to determine the mechanical properties such as the fiber volume fraction.

It can be concluded that the advantage of in-situ mechanical system using attenuation based x-rays for GFPP composites provides a nondestructive technique to visualize the fiber morphology and ability to predict zones of fracture. For future experiments, a higher optical magnification is required (500x-1000x) to view the cracks and damage evolution of the composite. This will allow observation of mechanical deformation including fiber pull-out, fiber volume fraction redistribution, crack propagation, crazing, and fiber debonding. Also the duration of time during which time the displacement was held constant corresponding to tomography collection, will need to be significantly reduced to prevent a significant stress relaxation effects on the composite samples.

### 3.3.3 In-Situ Mechanical Tensile Testing System using Digital Optical Microscopy

The Keyence VHX-600 digital microscope developed by Keyence, Inc. ([www.keyence.com](http://www.keyence.com)) was used in this research. This digital microscope affords the

ability to view in real-time high resolution key features of interest on the surface of the composite samples by using color CCD camera high density pixels. Two GFPP (one fast-fill, one slow-filled) and two CFVE tensile samples were loaded using in-situ mechanical tensile system with an axial force capacity of 90 kN. The testing system uses custom developed LabView based data acquisition and control software for performing both stress and strain controlled tests. A very precise small load cell with full scale capacity of 111 N (25 lb-f) was used to carefully perform the tensile testing. An .avi video file, using Keyence digital image software, recorded the samples during tensile loading at a continuous rate until noting an abrupt drop in their amplitudes. At high magnification (500x-1000x), cracks could not be observed until the sample failed.

Typical experimental results for the GFPP shown in Figure 3.7 indicate brittle behavior and small changes in the initial stiffness corresponding to tensile Young's modulus for both fill rates. The state of stress corresponded to a failure decrease (engineering strain = 19%) for slow-filled GFPP compared to the fast-filled GFPP composite. This difference in mechanical failure may be attributed to manufacturing process effects on slow and fast-filled injection molded composites found in Part 1 [23]. The interpreted modulus suggest no significant changes in reported macroscopic stress-strain behavior of GFPP [37]. The tensile strength, strain to failure decreased with the use of the slow-fill rate indicating that a more brittle behavior when compared to the fast-fill case. It is interesting to note the considerable difference in mechanical behavior between the two samples after failure. The fast-filled composite (AF3D-3) tend to fail abruptly indicating fiber pull-out and the slow-filled composite (AS3I) appears to show

fiber debonding behavior corresponding to point C as shown in Figure 3.7. Due to the external stress applied to the slow-filled GFPP composite, the interfacial debonding is nonlinear due to the effect of the Poisson contraction of the fiber, subjected to uniaxial tension [38]. As shown in Figure 3.7, point D on the stress-strain curve for the slow-filled dogbone sample indicates that cracking of the matrix occurring in the fiber bundles oriented at other angles to the applied stress. This rapid change in the stress-strain curve slope is due to cracking between fiber bundles. As shown in Figure 3.7 it can be concluded for the tensile test data that the fast-filled GFPP composite sample indicates a higher strength but weaker interface, and the slow-filled GFPP composite is a tougher material however at the expense of strength.

Figure 3.8 shows a typical GFPP composite sample after failure. The composite failed due to debonding, fracture, and pullout behavior which these failure mechanisms indicate shear yielding and plastic deformation in the composite [39]. The fibers are randomly dispersed without preferred orientation. In the damage zones, the dominant mechanism is poor adhesion where the cracks toward the interface obstacle by the fibers. Hence, less energy is required to pullout due to poor adhesive interfacial strength. These observations agree with prior research that E-glass has a very poor interfacial adhesion for polypropylene [40]. Fiber breakage observed in the fracture zone where failure initiation in highly stress concentration areas, indicating the location of local crack propagation toward the end of the glass fibers. This behavior is consistent with prior research that glass fiber ends location for crack initiation sites [27]. In addition, the GFPP appears to have a poorly filled resin where the presence of cavities of the surface

can be seen. The failure pattern of the composite sample indicate the following: **i)** the mechanical failure can be attributed to the existence of longer fibers which restricts the matrix movement. **ii)** The individual fibers and matrix fail by fiber debonding and pull-out as can be observed. These largely smooth and clean glass fibers resulting from the fiber pull-out indicates poor adhesion and weak interface between the fiber and matrix [37]. **iii)** Since the interface of the fiber and matrix is weak then this is a shear stress concentration parallel to the fiber and matrix causing interfacial shear debonding [41]. **iv)** The fractured fiber ends and fiber debonding viewed in Figure 3.8, indicate regions here where the stress is largely concentrated, where near fiber ends, debonded areas of the interface of the fiber and matrix are formed at relatively lower levels of stress than the other regions of the composite [42]. **v)** Also, the bundles of fibers shown indicate factors such as low wettability and fiber-fiber contact during injection molding contributed to the failure.

It is worth addressing the low adhesion between the fiber and matrix interface for the GFPP composite specimen used in the present study. The failure behavior of the composite indicates poor interface shear strength in the sample. The void content and low interfacial strength may explain the lower modulus observed for slow-filled GFPP composite since it has significantly higher and low stress distribution compared to the relative consistent strength of the fast-filled sample. The injection molding temperature should be increased to decrease the void content which would decrease the fiber pull-out sites. In addition, decreasing the pellet fiber length from 12 mm may improve the mechanical properties of the composite specimen. Though it is intuitive to increase the

fiber lengths to improve the mechanical properties of the GFPP composite specimen, the 12 mm long pellets in injection molding used in this paper have a bending tendency during plastication, which leads to a decrease in tensile strength and modulus [42]. An increase in tensile strength and modulus was found to be effective up to 9 mm pellets for GFPP composite material [43].

Using a continuous loading technique for the GFPP composites significantly increase the modulus and yield strength as shown in Table 1. Although the surface of the composite provided good detail of the mechanical failure properties using digital microscopy, this method is limited to two dimensional observations. Compared to x-ray imaging, we are unable to view the fiber morphology beneath the surface to qualitatively evaluate changes in the microstructure of the glass fiber until after failure. In addition, although the microscope had 1000x optical magnification capability, it did not offer any unique observations above 500x. Hence, an improved light source is needed to view cracks that develop on the surface while under tensile loading. Future planned experiments will address these limitations by the use of SEM with high optical magnification to view the surface in high resolution.

Typically, the strength of carbon fibers are approximately twice that of glass fiber, however lower elastic modulus and tensile strength is expected for 45° oriented dogbone samples where the deformation mechanism is dominated by the effect of flaws in the matrix leading to fiber pull-out [44]. Figure 3.9 and Table 3.1 shows typical tensile stress-strain curves of CFVE composite samples, where the sample exhibit linear stress-strain behavior with plateau region indicating a progressive rather than catastrophe failure.

The stress then decrease rapidly after the plateau region for all three samples. After which the load drops with increasing displacement, an indication of brittle behavior, and finally forms a long tail due to fiber debonding and pullout. The moduli of the stress-strain curve for all three samples are close, although CFVE-2 has a higher proportional limit and a higher failure strain. CFVE-1 and CFVE-3 has similar ultimate strengths and may be lower than CFVE-2 due to manufacturing defects such a machining and curing, which leads to strength degradation. In addition, the curves exhibit curves exhibit a plateau-like shape beyond the proportional limit and the linear curves typical of brittle behavior. These data suggest that a rather significant weakening of the interface bond between the fiber and matrix from the alignment and manufacturing, which correlates fiber degradation of the fibers.

The stress-strain curve of CFVE-2 sample exhibits a stronger and tougher behavior than CFVE-1 and CFVE-3 samples. This observed increase in strength of CFVE-2 infers the load can still be transferred effective from matrix to carbon fiber, assuming its interfacial bond strength between fiber and matrix to be appropriate. The samples CFVE-1 and CFVE-2 using the digital microscope (CFVE-3 is discussed in the next section) similarly to the GFPP composites, cracks could not be observed during the tensile testing from the viewing angle shown until after the samples failed. In Figure 3.10 and Figure 3.10b, typical failure pattern of the CFVE samples show several fibers are present during the pull-out because the high concentration of the fibers which leads to damaged fibers that are perpendicular to crack propagation directions [45]. Figure 3.10a and Figure 3.10b shows the morphology of the carbon fiber, where long fiber pullout is observed

indicating moderately weak interfacial strength. Furthermore as shown in Figure 3.10a and Figure 3.10b, the smooth and clean fibers indicate a weak adhesion of the vinyl resin to carbon fibers which is not surprising since there are known issues of carbon fiber not adhering to the vinyl resin well [44]. Fig 10a shows local strongly bonded and misaligned fibers indicating there is stress and strain magnification in the matrix which is maximum between the fibers corresponding to the plateau-like region and “knees” as shown in Figure 3.9. The 45° fibers are misaligned after pullout, which suggest the fiber-matrix bonding may have been dramatically lowered and fibers significantly weakened from local weak adhesion between fiber and matrix. Beyond the elastic limit, the applied load results in uniform plastic deformation, till the maximum load is reached. As observed in Figure 3.10b, CFVE-1 failure did not fail along the 45° alignment of fibers, which may explain the lower bound modulus shown in Figure 3.9. The CFVE-2 sample failed along the 45° alignment which is typical for this [ ± 45, 2s] lay-up [33]. As shown in Figure 3.10c the fracture shown indicate that fibers aligned in the crack direction and adhesion interfacial failure for this results in a cleavage fracture. This cleavage fracture was cracking of the matrix obstructed by the carbon fibers. Figure 3.10c shows the microcracks which are formed in the rather narrow stress range corresponding to the plateau-like domain in the stress-strain curve of CFVE-1 (Figure 3.9), run across the thickness of the sample in planes roughly perpendicular to the load axis.

Although the surface of the stitched carbon vinyl resin in could be viewed in great detail, the limitation of the polarized light and optical magnification prevented observation of the crack developing for the CFVE composite samples. The limitations

included two dimensional projection of the video, and limited viewing angle having the inability to rotate the sample to different view angles in order to observe cracking of the CFVE sample in real-time. For future planned experiments, non-destructing testing such as Micro-XCT would be needed to view any possible defects in the CFVE composite and predict damage zones using failure criterion such as fiber morphology and fiber volume fraction.

#### 3.3.4 In-situ Mechanical Tensile Testing using Large Chamber Scanning Electron Microscope (LC-SEM)

The LC-SEM manufactured by VisiTec ([www.visitec.com](http://www.visitec.com)) shown in Figure 3.11 was used to investigate the CFVE-3 sample to obtain micro-structured features of importance, including the evolution of damage and microstructural features as a function of mechanical stress. The CFVE-3 sample was loaded using the above mentioned in-situ tensile testing system used for digital microscopy and vacuum suitable for LC-SEM testing. A load cell with a full scale capacity of 3336.2 N (750 lb-f) was used for the tensile testing. As shown in Figure 3.11, the LC-SEM is equipped with the following: secondary electron detector, backscattered electron detector (4 quadrants), energy dispersive x-ray spectrometry (EDS), and variable pressure mode. In-situ LC-SEM affords the ability of testing larger specimens having geometry and dimensions similar to those used in traditional mechanical testing laboratories. The LC-SEM eliminates the need for using artificially small specimens, reducing unwanted size effects associated with applied deformation on the microstructure. Deformation mechanisms, such as crack propagation, as well as other microscopic features, such as fiber debonding, and matrix

yielding were examined in-situ under tensile stress at desired magnifications ranging from 125x to 10,000x. Similar to the digital microscopy method, a video using digital image software was recorded the sample while under tensile loading at constant displacement rate until mechanical failure of the sample.

In order to find the mechanism of fracture, Figure 3.12(a-d) represents optical micrographs captured while under uniaxial tensile loading. The corresponding load-displacement curve is shown in Figure 3.13. Figure 3.12 shows gage length area of the CFVE-3 sample where the damage evolution can be qualitatively evaluated. As shown in Figure 3.12a, the white patches are vinyl ester resin and the dark region represented the carbon fiber concentration of the composite sample. These white patch features suggest these zones has already undergone some degradation during the curing and manufacturing of the sample thus allowing more decohesion to occur between the fibers and the matrix. Hence, the white patches are indication of failure initiation and final fracture zones leading to pre-mature fracture during a tensile test [33]. Initial failure is shown in Figure 3.12b, where resin cracking was first noticed at 305 N tensile loading as at point O indicates where the load transferred to the fibers has peaked. Five additional cracks appear on the surface as this crack propagated weakening the fiber and matrix interface causing the crack to at point P to appear as shown in Figure 3.12c. These microcracks shown in Figure 3.12b and Figure 3.12c suggest the crack propagated or “followed” along the fiber matrix interface in regions of the dense packing of fibers, where it can be seen that many initial cracks were generated simultaneously where the damage occurs almost instantaneously. This indicates isolated interfacial cracks that grow

and connect as the tensile load is increased [34]. Furthermore, this cracking from the applied load is progressively transferred to the fibers up to composite failure which occurs at a strain. As shown in Figure 3.12c, the matrix microcracking corresponding to the plateau region indicates that the fibers, which are now largely debonded from the matrix, carry the applied load alone and the failure occurs. The microcracking results in abrupt failure of the composite as shown in Figure 3.12d.

Interfacial failure is the dominating failure mechanism for this sample and the features are illustrated in Figure 3.12c and Figure 3.12d. These cracks shown in Figure 3.12c and Figure 3.12d indicate that debonding of the fiber from matrix probably begin before the plateau-like region show in Figure 3.13 is reached. As shown in Figure 3.13, the plateau region indicates that the fiber and matrix interface could not sustain any additional load. The debonding is the Poisson contraction of the carbon fiber against the matrix cure shrinkage, assuming that the fiber did not break first. It is interesting to note since the carbon fibers are aligned  $45^\circ$  to the tensile axis, the width of the gage length area is decreased from this alignment approaching 305 N loading, although the maximum load is still in the proportional limit. A possible reason for this failure mechanism is due to the local strongly bonding between the fiber and matrix effective carry the shear load across the gage length.

The cracking of the matrix occurs while under tensile load and the width of the observed cracks increases with increase in the applied load together debonding and pullout of the fibers from the matrix as shown in Figure 3.12d. This weakening corresponding to plateau region and long tail can viewed on the stress-strain curve as

shown in Figure 3.13. As shown in Figure 3.12d and Figure 3.13, beyond point D the pullout is only under the resistance of friction appear to correspond to the drop following the plateau-like region.

It is worth noting, the cracks developed around the white patches confirming these were crack failure initiation sites as predicted. The LC-SEM experimental test successfully shows the damage evolution as a function of the tensile loading correlating the load-displacement curve and micrographs. As shown in Figure 3.14a and Figure 3.14b, the fracture surface after failure was investigated using LC-SEM to qualitatively evaluate the interfacial debonding. In this case locally small pullout is observed and matrix appears between the fibers, which may be inferred that the fiber-matrix interfacial bond is strong locally. Using SEM microscopy show degraded mechanical properties based on a local bonded interface and degradation of fibers due to machining. As shown in Figure 3.14, it can be clearly seen that the interface failed. The damage pattern of the sample is shown where typical fracture surface for a specimen with 45° fiber orientation were caused by fracture micromechanics resulting from interfacial debonding in the carbon fiber/vinyl ester. The matrix plastically deformed locally allowing fibers to bridge the matrix crack more aligned to the tensile axis corresponding to the plateau region and pullout regions in Figure 3.13. In addition, the cracks tend to run along the matrix between the fibers which indicate a brittle microstructure for the composite specimen. Figure 3.14a shows smooth and clean carbon fibers although having local areas of strong interfacial adhesion. This indicate local matrix near the interface between the fiber and matrix failed. SEM evaluation indicates the dominating mechanism is

adhesive failure for weaker interface and cohesive failure for the strong interface. On fracture, corresponding beyond the elastic limit of the load-displacement curve, the matrix which is porous and cracked gets disintegrated leaving the fibers exposed. The brittle behavior corresponding to the region following point D in Figure 3.13, the local yielding forming the long tail from pullout as shown in Figure 3.14a. As shown in Figure 3.14b the fractured surface of an individual fiber using high magnification (10000x) can be observed indicating the brittle behavior of the CFVE sample caused by fiber pull-out.

Since the effective load carried by the fibers depends primarily on their strength and effective area, improvements in adhesion will be needed to provide suitable fiber-matrix interfacial bonding for effective transfer of load from matrix to fibers. Due to limitation of one viewing angle, it is unknown whether resin cracking, crack propagations occurred on the other side of the gage length area.

Although the cracks development and microstructure of the surface of the CFVE sample was observed in great detail, similar to the digital microscopy experiment, the limitations are the restricted two dimensional viewing and destroying the sample in order to view the fiber and matrix interface. Future planned experiments would be able to rotate the sample using a rotating stage to view different sides of the gage length area. In addition, the CFVE samples should be coated to prevent charging, lower the use of the voltage (below 1 keV) or test at variable pressure [25].

### **3.4 Conclusion**

Three unique in-situ experimental tensile system using Micro-XCT, digital microscopy, and LC-SEM were used to investigate the microstructure of the E-glass fiber

with polypropylene resin and carbon fiber with vinyl ester resin composites while under tensile loading. Changes in microstructure beneath the surface of the GFPP composites was able to be observed under loading, however due to geometric magnification limitation cracks in the matrix and fiber was not able to be observed. Radiograph and tomography collection caused stress relaxation which significantly reduce the strength of the GFPP composites. Using digital microscopy cracks were not able to be observed during tensile testing. However, key features of interest such as fiber pull-out, fiber bundling, fracture fiber ends were observed from failure for both GFPP and CFVE composites. The dominant failure mechanism for GFPP was low adhesion between the fiber and matrix. SEM provided unique observation of the stress damage evolution was successfully observed on the surface of the CFVE composite where crack initiation and crack propagation while the sample was under tensile loading. The dominant failure mechanism for CFVE samples was interfacial failure.

## **REFERENCES**

- [1] Nguyen BN, et al. Fiber Length and Orientation in Long-Fiber Injection-Molded Thermoplastics Part 1: Modeling of Microstructure and Elastic Properties. *Journal of Composites Materials* 2008; 42: 1003-1029.
- [2] Hashin Z. The Elastic Moduli of Heterogeneous Materials. *Journal of Applied Mechanics* 1962; 29: 143-150.
- [3] Christensen RM. *Mechanical Properties of Composite Materials*. John Wiley, New York: 1979a.
- [4] Matthews FL, Rawlings RD. *Composites materials: Engineering and Science*. Woodhead Publishing Limited, Cambridge: 1999.
- [5] Montsinger LV. Thermoplastic Composite Made by Rotational Shear. U. S. Patent 6,258,453: 2001.
- [6] Velez-Garcia G, Kunc V. Experimental Methods to Evaluate Fiber Length and Orientation Distribution of Long Glass Fibers in Injected Molded Thermoplastics. Fiber Society Conference, Knoxville, Tennessee. October 10-12, 2006.
- [7] Homayonifar M, Zebarjad SM. Investigation of the effect of matrix volume on fiber stress distribution in polypropylene fiber composite using a simulation method. *Materials and Design*. 2007; 28: 1386-1392.
- [8] Davidson NC, Clarke AR. Extending the dynamic range of fibre length and fibre aspect by automated image analysis. *Journal of Microscopy*. 1999; 196: 266-272.
- [9] Eberhardt CN, Clarke AR. Automated reconstruction of curvilinear fibres from 3D datasets acquired by X-ray microtomography. *Journal of Microscopy*. 2002; 206: 41-53.

- [10] Scott D, et al. High Resolution 3D Tomography for Advanced Package Failure Analysis White Paper. Xradia, Inc. Concord, CA.
- [11] Patcharaphun S, Mennig G. Properties Enhancement of Short Glass Fiber-Reinforced Thermoplastics via Sandwich Injection Molding. *Polymer Composites*. 2005; 26: 823-831.
- [12] Stock SR. X-Ray Methods for Mapping Deformation and Damage. In *Micromechanics – Experimental Techniques*. J.W.D. Sharpe (Ed.) ASME. AMD. 1990; 102: 147-162.
- [13] Kak C, Slaney M. *Principles of Computerized Tomographic Imaging*. IEEE Press: 1988.
- [14] Banhart J. *Advanced Tomographic Methods in Materials Research and Engineering*. Oxford University Press, New York: 2008.
- [15] Cann MT, Adams DO, and Schneider, CL. Characterization of Fiber Volume Fraction Gradients in Composite Laminates. *Journal of Composite Materials* 2008; 42(5): 447-466.
- [16] Ota WN, Amico SC, Satyanarayana KG. Studies on the combined effect of injection temperature and fiber content on the properties of polypropylene-glass fiber composites. *Composites Science and Technology* 2005; 65: 873-881.
- [17] Fu SY, et al. Fracture behavior of short glass fiber and short carbon fiber reinforced polypropylene composites. *Int. J. of Materials and Product Technology* 2002; 17(1/2): 108-120.

- [18] Zebarjad SM, et al. Role of the interface on the deformation mechanism of glass fiber/polypropylene composites. *Journal of Materials Science Letters* 2002; 21: 1007-1011.
- [19] Hashin Z, Herakovich CT. *Mechanical Properties of Composite Materials: Recent Advances*. Pergamon Press, New York: 1983.
- [20] Gol'dman AY, et al. *Prediction of the Deformation Properties of Polymeric and Composite Materials*. American Chemical Society, Washington, DC: 1994.
- [21] Xradia, Inc. "MicroXCT User's Manual 2.0 Issue 1.1" (2005).
- [22] Nguyen BN, Holbery JD, and Kunc V. *Engineering Property Prediction Tools for Tailored Polymer Composite Structures: FY 2005 Progress Report*. Oak Ridge National Laboratory, Oak Ridge, TN. Retrieved July 8, 2009 from [http://www1.eere.energy.gov/vehiclesandfuels/pdfs/alm\\_05/4k\\_nguyen.pdf](http://www1.eere.energy.gov/vehiclesandfuels/pdfs/alm_05/4k_nguyen.pdf)
- [23] Young S, Penumadu D, and Kunc V. *High Resolution X-ray Tomography of Chopped Fiber Polymeric Composites*. *Composites Science and Technology* (submitted).
- [24] Liu H, Liao K. *Tensile Behavior and Morphology Studies of Glass-Fiber-Reinforced Polymeric In Situ Hybrid Composites*. *Journal of Applied Polymer Science* 2004; 94: 211-221.
- [25] Lindhagen J, Bergund L. *Microscopial Damage Mechanisms in Glass Fiber Reinforced Polypropylene*. *Journal of Applied Polymer Science* 1998; 69: 1319-1327.

- [26] Plummer CJG, et al. Microdeformation in Heterogeneous Polymers, Revealed by Electron Microscopy . *Macromol. Symp.* 2004; 214: 97-114.
- [27] Zebarjad SM. The influence of glass fiber on fracture behavior of isotactic polypropylene. *Materials and Design* 2003; 24: 531-535.
- [28] Addiego F, Abdesselam D, G'Sell C, and Hiver JM. Characterization of volume strain at large deformation under uniaxial tension in high-density polyethylene. *Polymer* 2006; 47: 4387-4399.
- [29] Stock SR. Recent Advances in X-ray Microtomography Applied to Materials. *International Materials Reviews* 2008; 53(3): 129-181.
- [30] Eberhardt CN, Clarke AR. Automated Reconstruction of Curvilinear Fibers from 3D Datasets Acquired by X-ray Microtomography . *Journal of Microscopy* 2002; 206(1): 41-53.
- [31] Davies R. J., et. al. The Use of Synchrotron X-ray Scattering Coupled with In Situ Mechanical Testing for Studying Deformation and Structural Change in Isotactic Polypropylene. *Colloid Polym Sci* 2004; 282: 854-866.
- [32] Stribeck N, Nochel U, Funari SS, and Schubert T. Tensile Tests of Polypropylene Monitored by SAXS. Comparing the Stretch-Hold Technique to the Dynamic Technique. *Journal of Polymer Science: Part B: Polymer Physics* 2008; 46: 721-726.
- [33] Shivakumar KN. Carbon/vinyl ester composites for enhanced performance in marine applications. *J. Reinf Plast Comp* 2006; 25(10): 1101-1116.

- [34] Hobbiebrunken T, Hojo M, Adachi T, De Jong C, and Fiedler B. Evaluation of Interfacial Strength in CF/epoxies Using FEM and In-Situ Experiments. *Composites: Part A* 2006; 37: 2248-2256.
- [35] Cardon AH. *Recent Developments in Durability Analysis in Composite Systems*. Taylor and Francis, New York: 2000.
- [36] Rizov V, et al. Fracture Toughness of Discontinuous Long Glass Fiber Reinforced Polypropylene: An Approach Based on a Numerical Prediction of Fiber Orientation in Injection Molding. *Polymers and Polymer Composites* 2005; 13(2): 121-130.
- [37] Zebarjad SM. Investigation of deformation mechanism in polypropylene/glass fiber composite. *Journal of Applied Polymer Science* 2003; 87(13): 2171-2176.
- [38] Kim JK, Mai YW. *Engineering Interfaces in Fiber Reinforced Composites*. Elsevier, New York: 1998.
- [39] Kumar KS, Bhatnagar N, and Ghosh AK. Mechanical Properties of Injection Molded Long Fiber Polypropylene Composites, Part 2: Impact and Fracture Toughness. *Polym. Compos* 2008; 29: 525-533.
- [40] Tselios CH, Bikiaris D, Savidis P, and Panayiotou C. Glass-fiber Reinforcement of In Situ Compatibilized Polypropylene/Polyethylene Blends. *Journal of Materials Science* 1999; 34: 385-394.
- [41] Li H. Stress transfer and damage evolution simulations of fiber-reinforced polymer-matrix composites. *Materials Science and Engineering A-Structural Materials Properties Microstructure and Processing* 2006; 425(1-2): 178-184.

- [42] Kumar, KS et al. Mechanical Properties of Injection Molded Long Fiber Polypropylene Composites, Part 2: Impact and Fracture Toughness. *Polym. Compos.* 2008; 29: 525-533.
- [43] Kumar KS, et al. Development of long glass fiber reinforced composites: Mechanical and morphological characteristics. *Journal of Reinforced Plastics and Composites* 2007; 26(3): 239-249.
- [44] Wonderly C, et al. Comparison of mechanical properties of glass fiber/vinyl ester and carbon fiber/vinyl ester composites. *Composites Part B-Engineering* 2005; 36(5): 417-426.
- [45] Fu, SY. Combined effect of fiber content and microstructure on the fracture toughness of SGF and SCF reinforced polypropylene. *Journal of Materials Science* 2002; 37: 3067-3074.
- [46] Sawyer, LC, et al. *Polymer Microscopy: Characterization and Evaluation of Materials*. Alden Press, Oxford: 1996

## **APPENDIX**

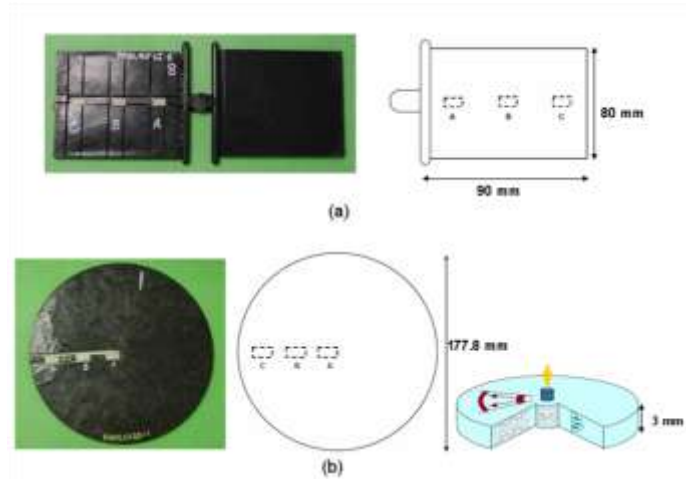


Figure 2.1: Schematic of the 3 mm thick pellet injection molding of E-glass fiber/polypropylene (a) ISO-plaque and (b) center-gated disk [1, 22].

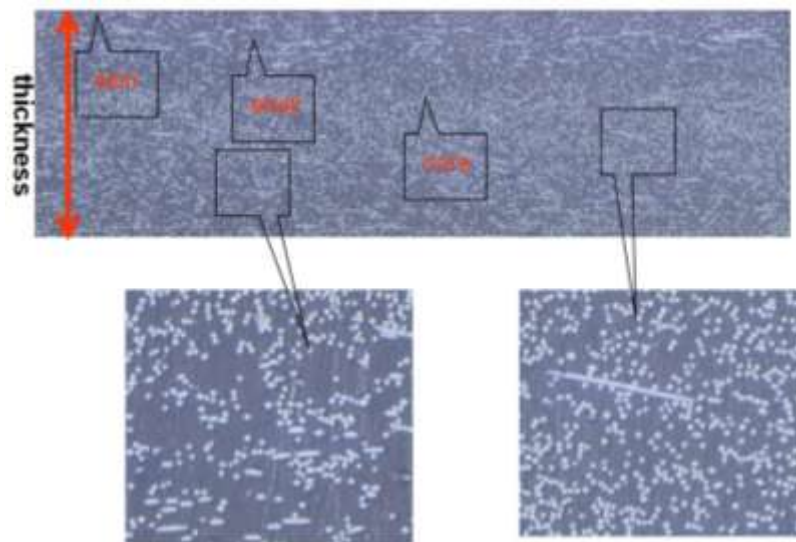


Figure 2.2: Schematic diagram of the skin, shell, and core layers of the E-glass fiber polypropylene molding compound at 50x magnification [6].

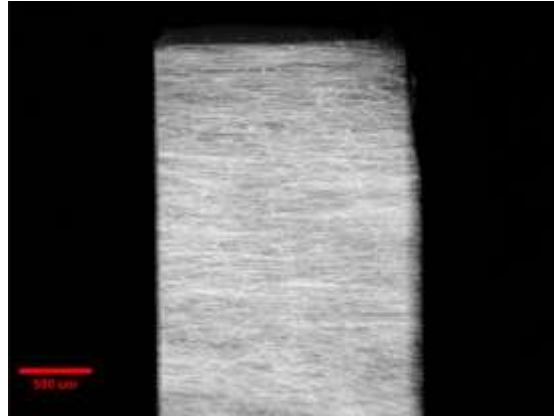


Figure 2.3: Radiograph of an absorption Radon transform projection of the E-glass fiber with polypropylene matrix at 4x magnification.

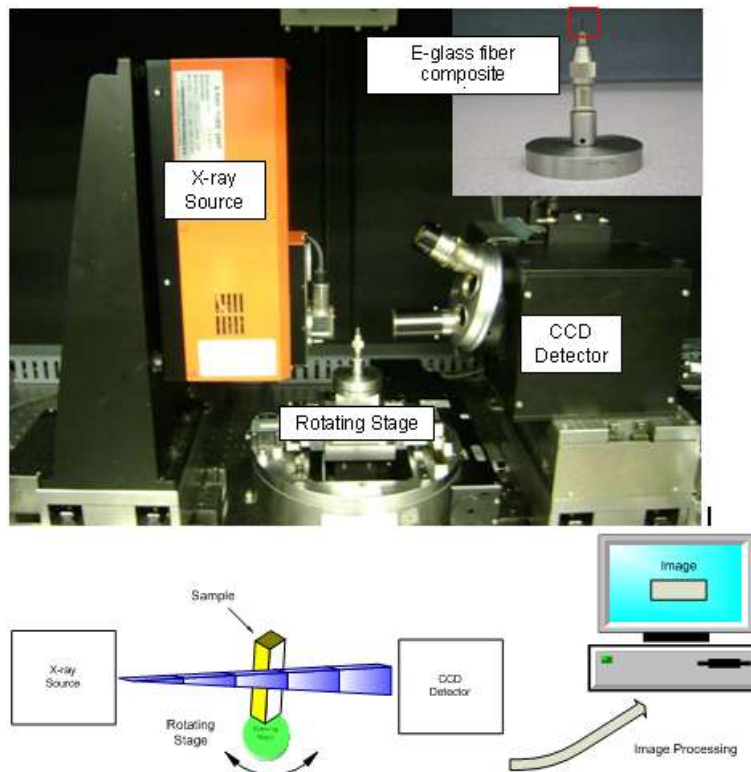
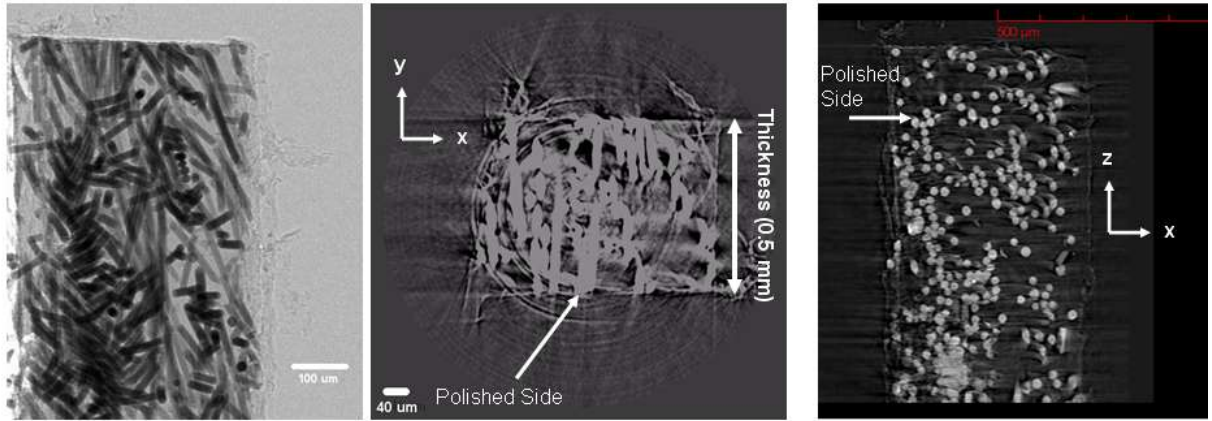


Figure 2.4: Illustration of tomography raw image collection. E-Glass fiber with polypropylene matrix composite sample (0.5 mm x 0.5 mm x 10 mm) inside sample holder. The X-ray source (100 kV, 10 W) and thermoelectrically cooled scintillation CCD detector (2048 x 2048 pixels, 16 bit) at -59 °C with fast readout scintillation crystal.

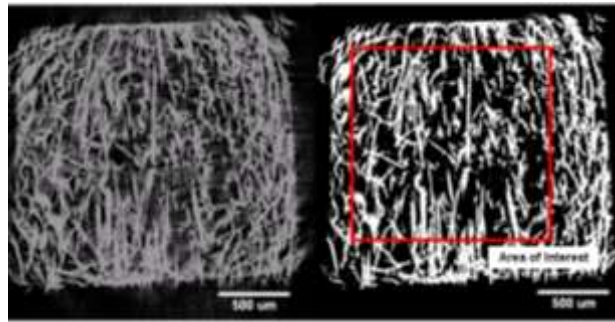


(a)

(b)

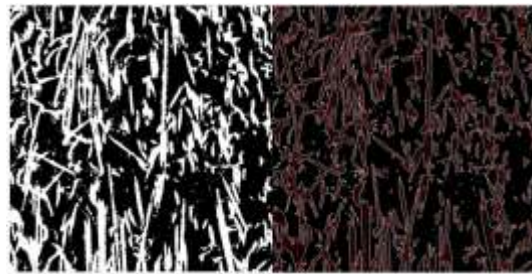
(c)

Figure 2.5: (a) Radiograph x-ray at 20x, and (b-c) 2D reconstruction slices of the cross section.



(a)

(b)



(c)

(d)

Figure 2.6: (a-b) 8-bit grayscale tomography reconstruction and corresponding thresholded image of E-glass fiber with polypropylene matrix composite sample.

(c-d) Thresholded and measured E-glass fibers in the area of interest.

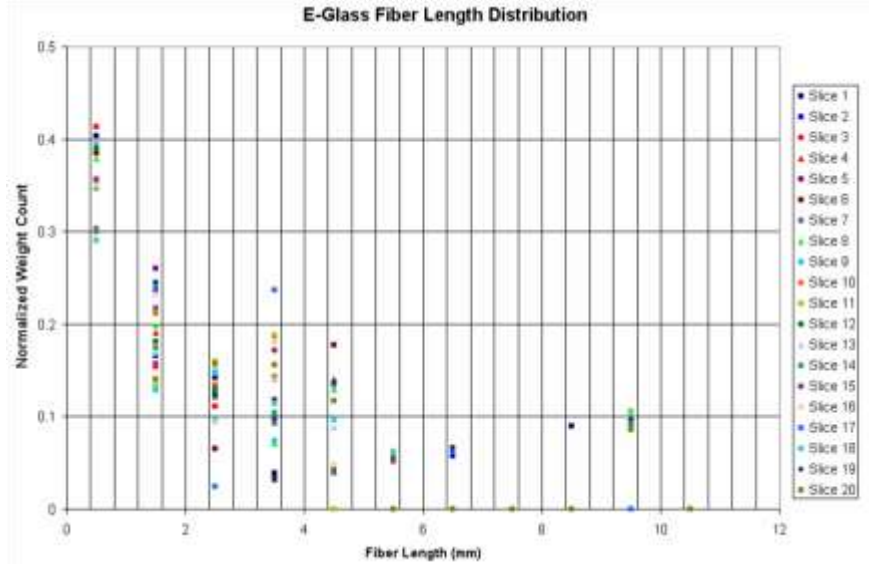


Figure 2.7: Fiber Length Distribution of E-glass fibers in polypropylene matrix.

**Area Density of Reconstructed Slices for  
E-glass Fibers with Polypropylene Matrix**

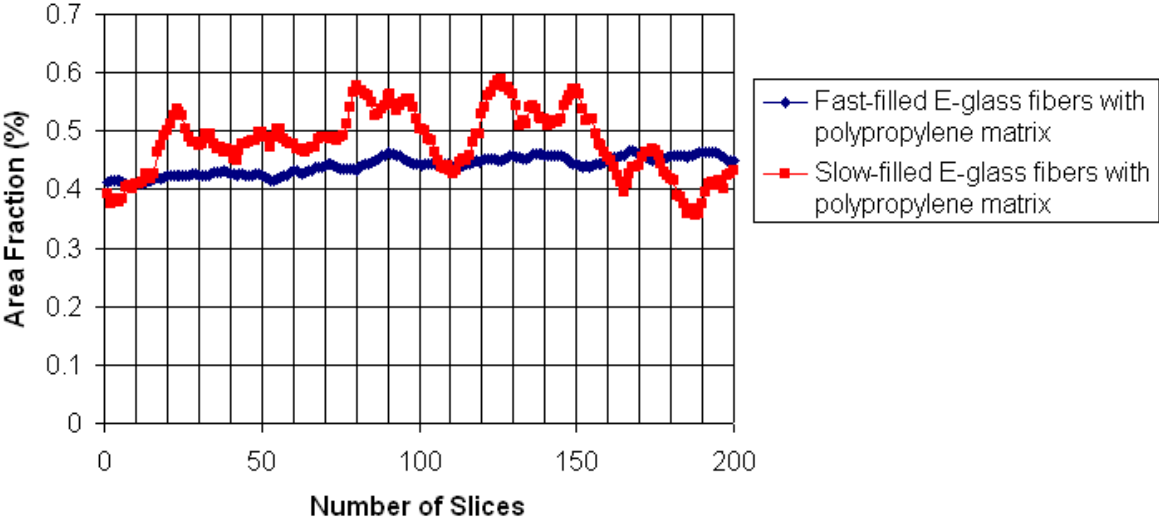


Figure 2.8: Area Density Distribution for fast-filled and slow-filled E-glass fibers in polypropylene matrix.

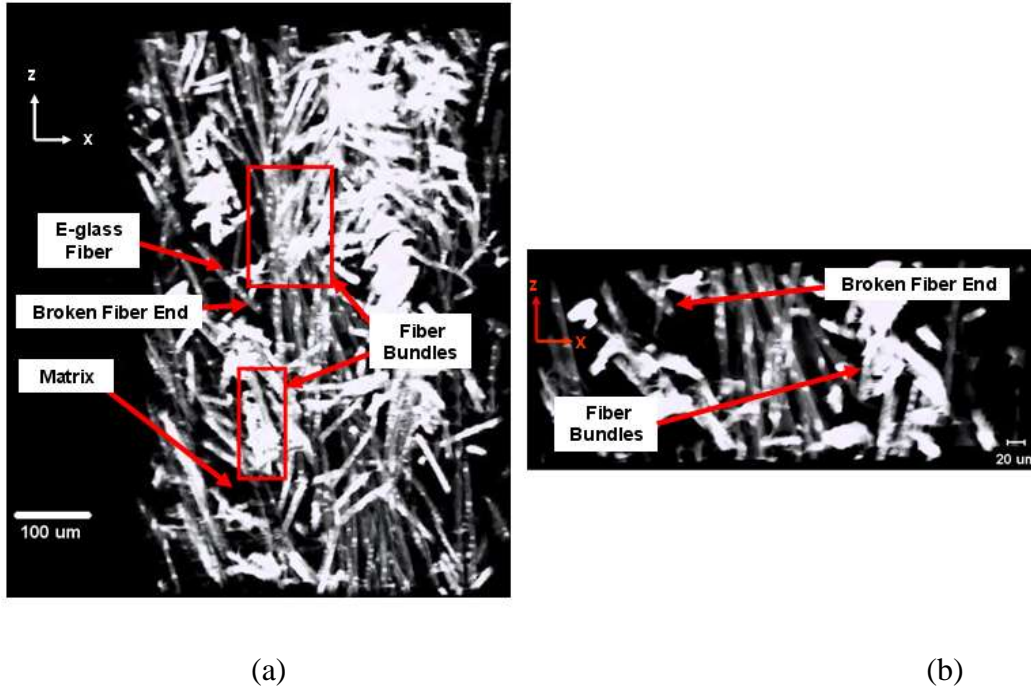


Figure 2.9 (a,b) 3D reconstructed images of the E-glass fiber with polypropylene matrix.

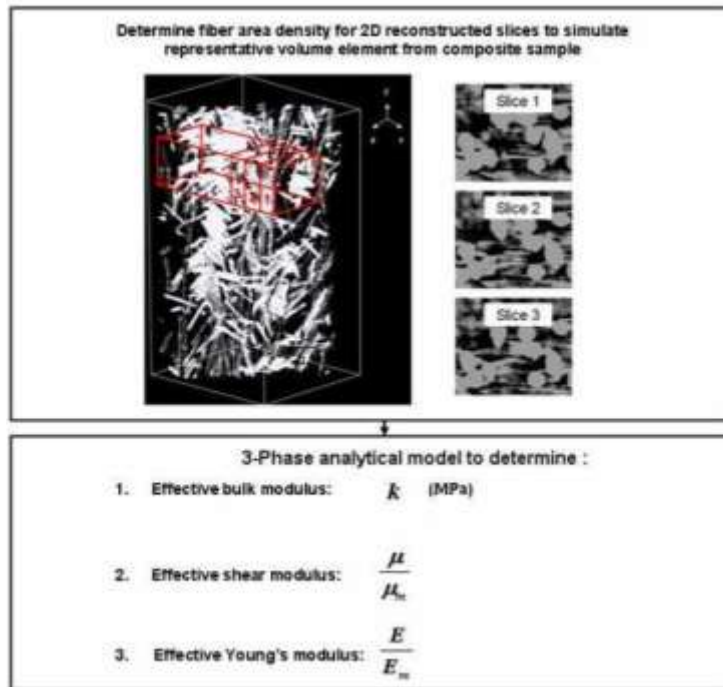
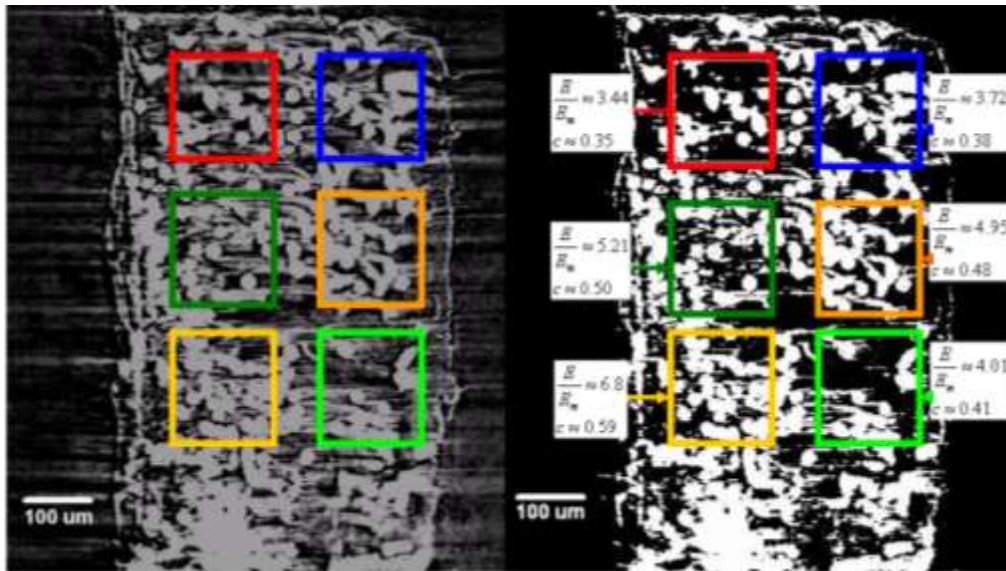
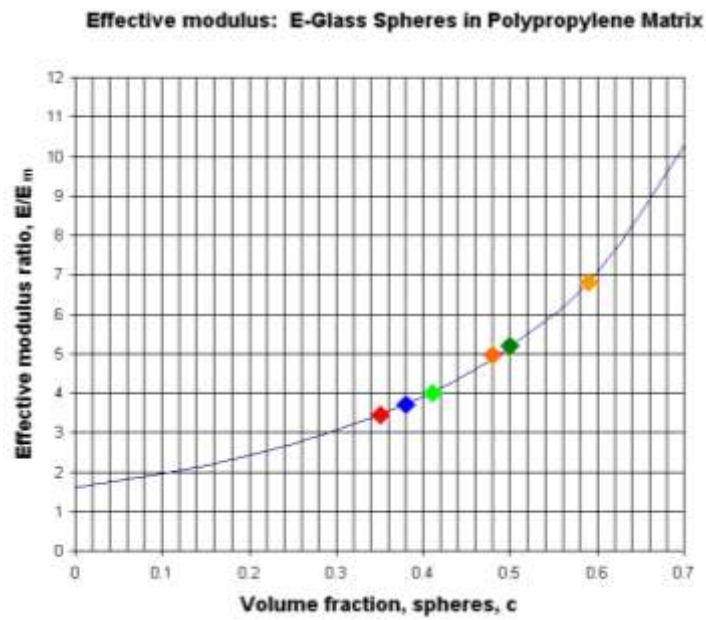


Figure 2.10: Flow chart to determine effective moduli for the E-glass fiber in polypropylene matrix.



(a)

(b)



(c)

Figure 2.11: (a) 8-bit grayscale tomography reconstruction, (b) corresponding thresholded image and (c) effective modulus for slow-filled E-glass fiber with polypropylene.

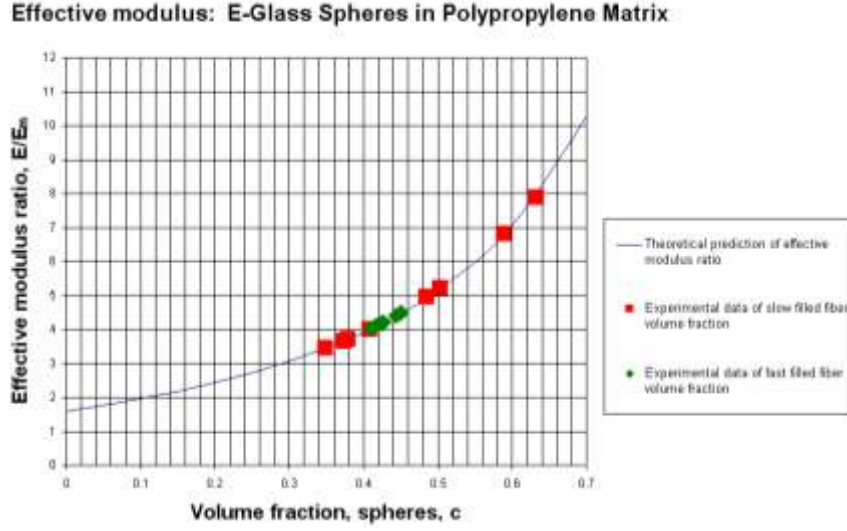


Figure 2.12: Effective modulus, E-glass spheres in polypropylene matrix

### A.1 3-Phase Model

The 3-phase model is derived from Christensen and Lo's model [3]. The solution for the effective shear modulus,  $\frac{\mu}{\mu_m}$ , is given by the solution of the quadratic equation shown in

Eq. 4 where subscript  $m$  refers to the matrix and constants  $A$ ,  $B$ ,  $C$  are defined by the following relationships:

$$A = 8 \left( \frac{\mu_i}{\mu_m} - 1 \right) \left[ 1 - 5\nu_m \bar{\eta}_1 c^{10/3} - 2 \left[ 63 \left( \frac{\mu_i}{\mu_m} - 1 \right) \eta_2 + 2\eta_1 \eta_3 \right] c^{7/3} \right. \\ \left. + 252 \left( \frac{\mu_i}{\mu_m} - 1 \right) \eta_2 c^{5/3} - 50 \left( \frac{\mu_i}{\mu_m} - 1 \right) (7 - 12\nu_m + 8\nu_m^2) \eta_2 c + 4(7 - 10\nu_m) \eta_2 \eta_3 \right] \quad (6)$$

$$B = -2 \left( \frac{\mu_i}{\mu_m} - 1 \right) \left[ 1 - 5\nu_m \bar{\eta}_1 c^{10/3} - 2 \left[ 63 \left( \frac{\mu_i}{\mu_m} - 1 \right) \eta_2 + 2\eta_1 \eta_3 \right] c^{7/3} \right. \\ \left. - 252 \left( \frac{\mu_i}{\mu_m} - 1 \right) \eta_2 c^{5/3} - 75 \left( \frac{\mu_i}{\mu_m} - 1 \right) (3 - \nu_m) \eta_2 \nu_m c + \frac{3}{2} (15\nu_m - 7) \eta_2 \eta_3 \right] \quad (7)$$

$$C = 4 \left( \frac{\mu_i}{\mu_m} - 1 \right) \left[ 5v_m - 7 \frac{\mu_i}{\mu_m} c^{10/3} - 2 \left[ 63 \left( \frac{\mu_i}{\mu_m} - 1 \right) \eta_2 + 2\eta_1 \eta_3 \right] c^{7/3} \right. \\ \left. + 252 \left( \frac{\mu_i}{\mu_m} - 1 \right) \eta_2 c^{5/3} + 25 \left( \frac{\mu_i}{\mu_m} - 1 \right) (v_m^2 - 7) \eta_2 c - (7 + 5v_m) \eta_2 \eta_3 \right] \quad (8)$$

with

$$\eta_1 = (49 - 50v_i v_m) \left( \frac{\mu_i}{\mu_m} - 1 \right) + 35 \frac{\mu_i}{\mu_m} (v_i - 2v_m) + 35(2v_i - v_m) \quad (9)$$

$$\eta_2 = 5v_i \left( \frac{\mu_i}{\mu_m} - 8 \right) + 7 \left( \frac{\mu_i}{\mu_m} + 4 \right) \quad (10)$$

$$\eta_3 = \frac{\mu_i}{\mu_m} (8 - 10v_m) + (7 - 5v_m) \quad (11)$$

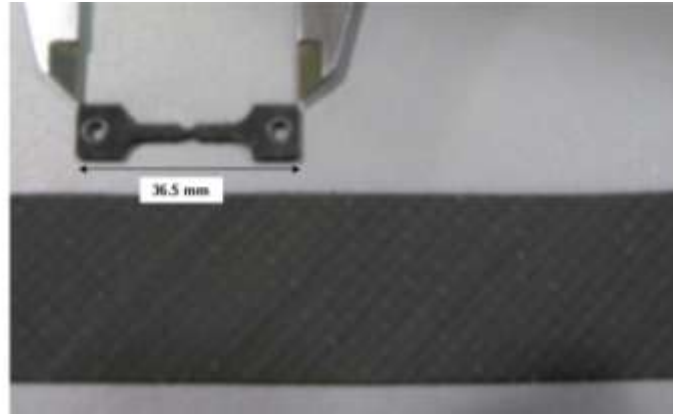


Figure 3.1: Schematic of the 3 mm thick,  $45^\circ$  [ $\pm 45$ , 2s] carbon fiber with vinyl ester resin and tensile sample.

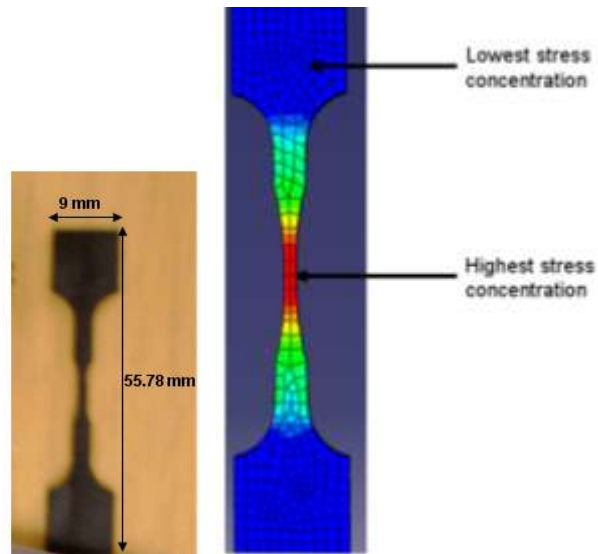


Figure 3.2: Schematic of (a) E-glass fiber/polypropylene dogbone composite sample and (b) corresponding finite element analysis stress concentration distribution.

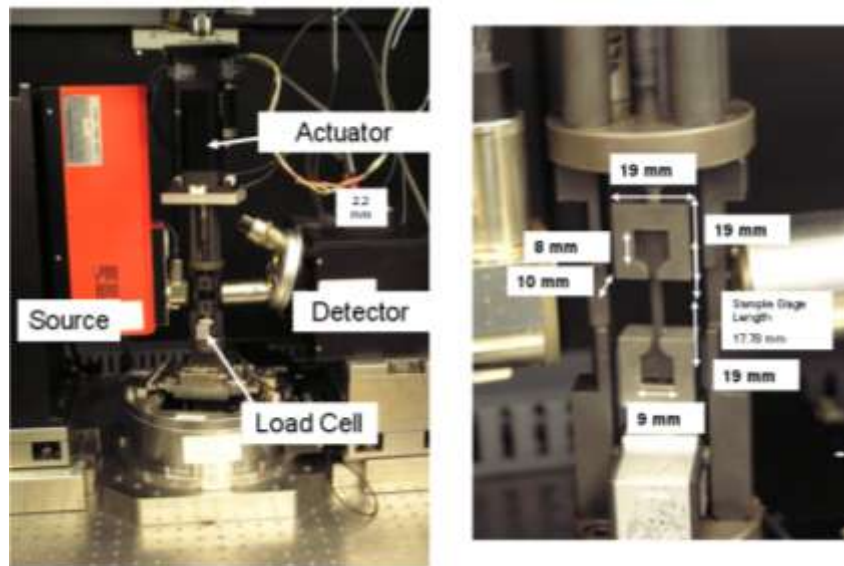


Figure 3.3: In-situ mechanical tensile system with actuator and 1334.5 N (300 lbf) load cell. E-Glass fiber with polypropylene matrix composite sample (2.3 mm x 1.4 mm x 55.78 mm) inside sample holder. The X-ray source (100 kV, 10 W) and thermoelectrically cooled scintillation CCD detector (2048 x 2048 pixels, 16 bit) at -59 °C with fast readout scintillation crystal.

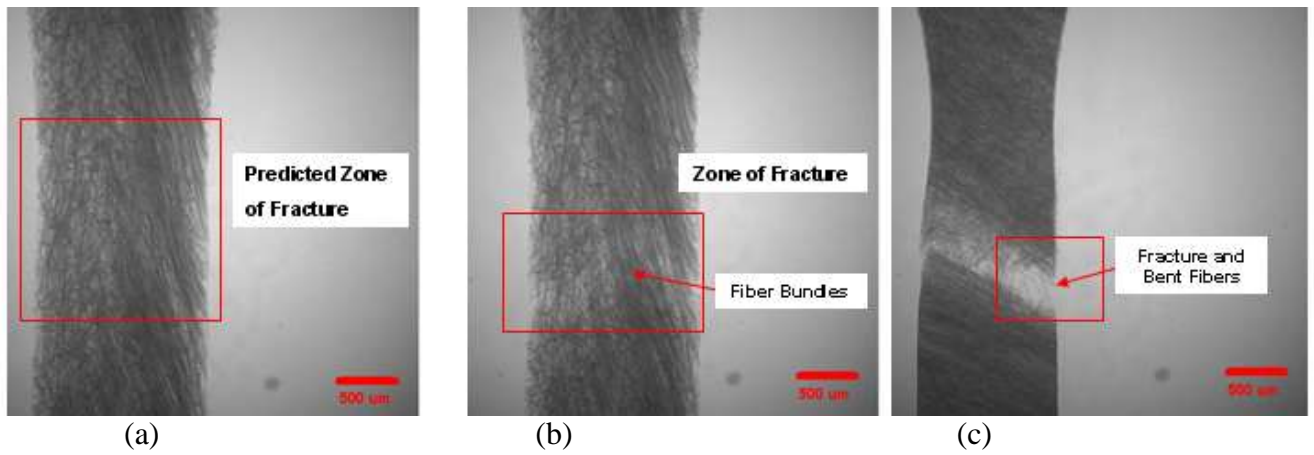


Figure 3.4: Radiograph of transmission Radon transform projection of the E-glass fiber with polypropylene matrix at 4x magnification (a) before tensile loading (b) during tensile loading and (c) after failure of the tensile sample.

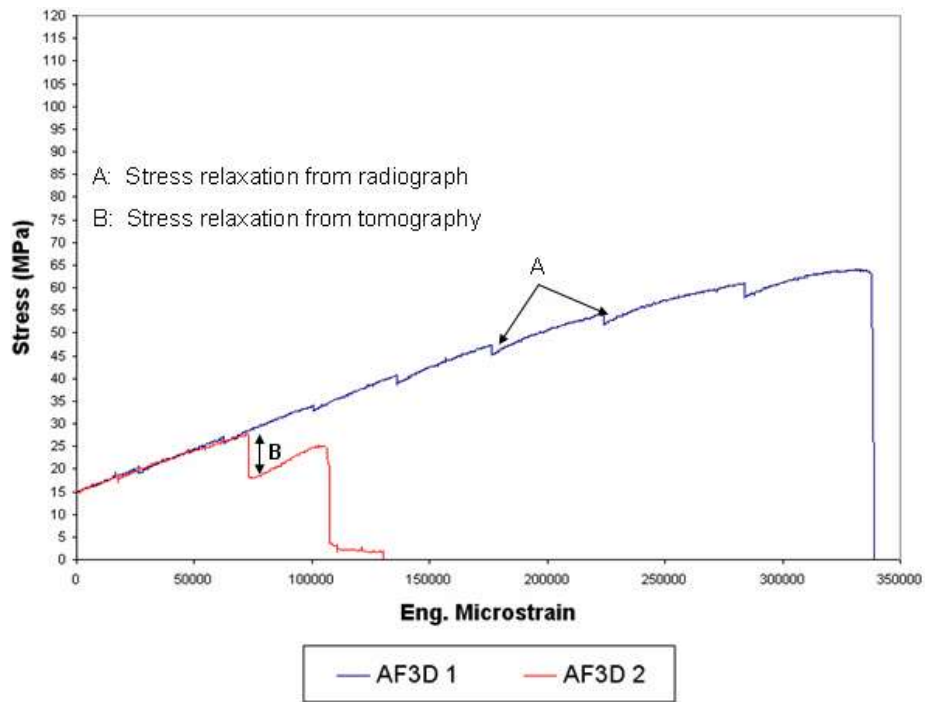


Figure 3.5: Experimental data corresponding to fast-filled E-glass fiber with polypropylene dogbone sample.

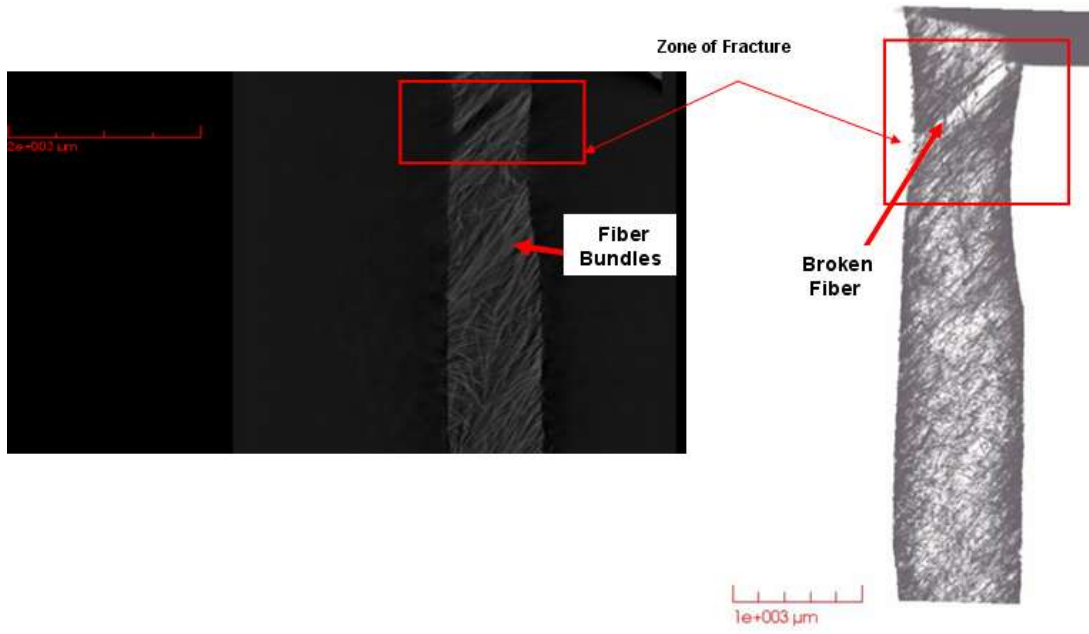


Figure 3.6: (a) 2-D reconstruction of E-glass fiber with polypropylene resin and (b) corresponding 3-D volumetric rendering after tensile loading.

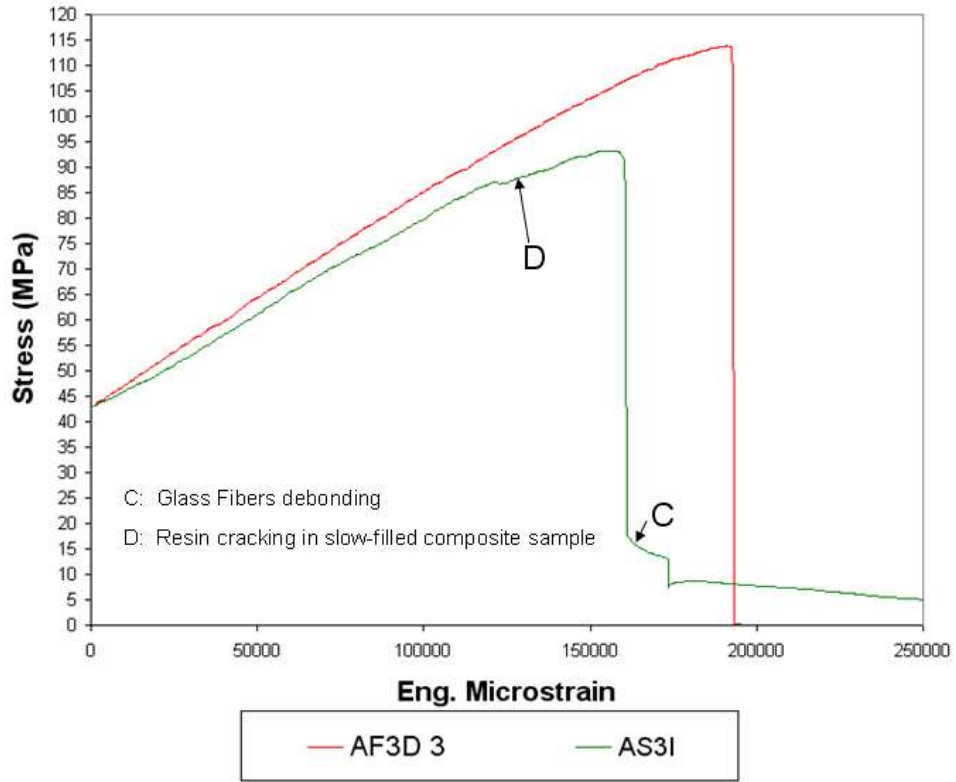


Figure 3.7: Typical experimental data for a tensile test for E-glass/polypropylene.

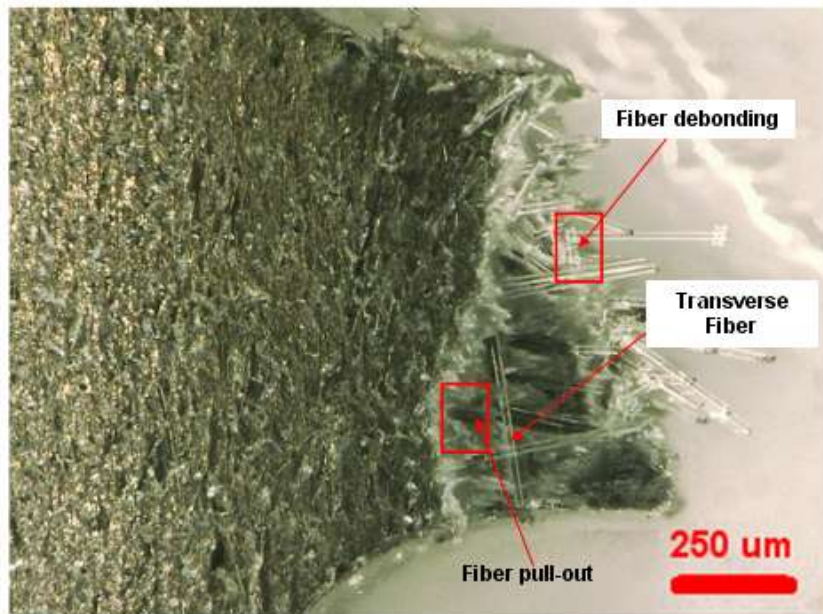


Figure 3.8: Fracture surface of E-glass with polypropylene resin after tensile failure.

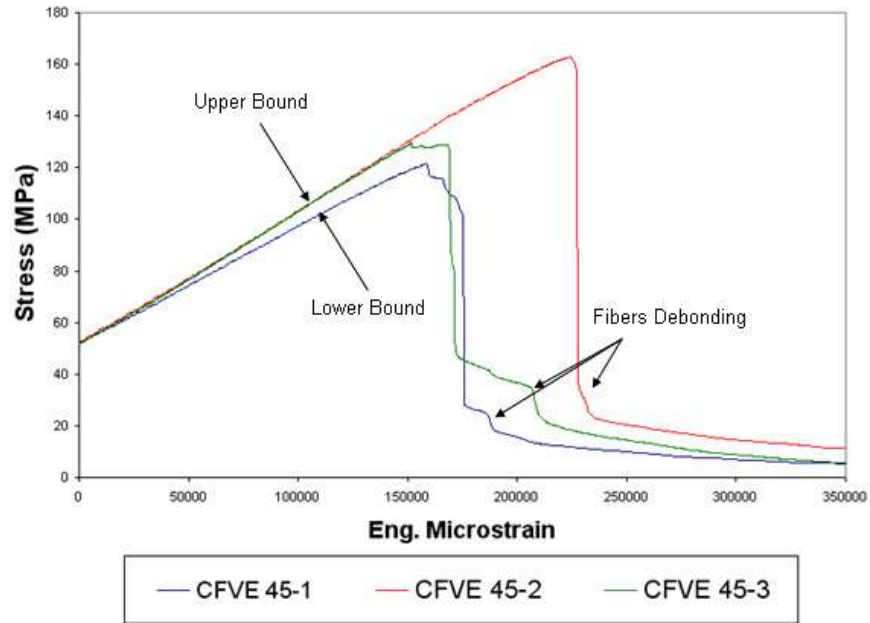
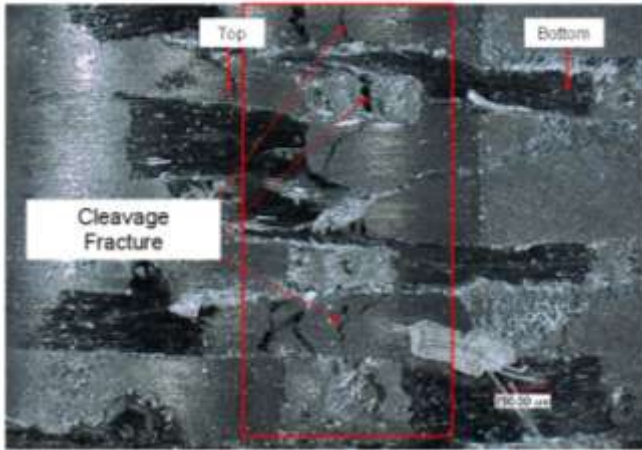


Figure 3.9: Typical experimental data for a tensile test for carbon fiber with vinyl ester resin.





(c)

Fig 3.10: Fracture surface of carbon fiber/vinyl ester after tensile failure for (a,b) by fiber pullout and (c) cleavage fracture.

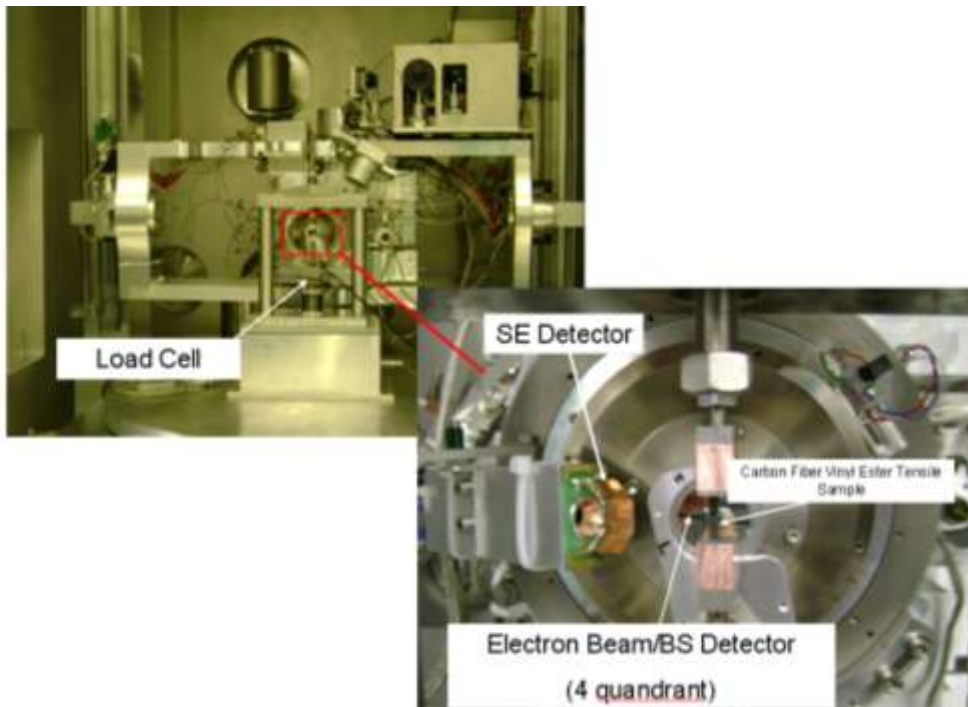


Figure 3.11: Experiment setup for the in-situ mechanical system in LC-SEM.

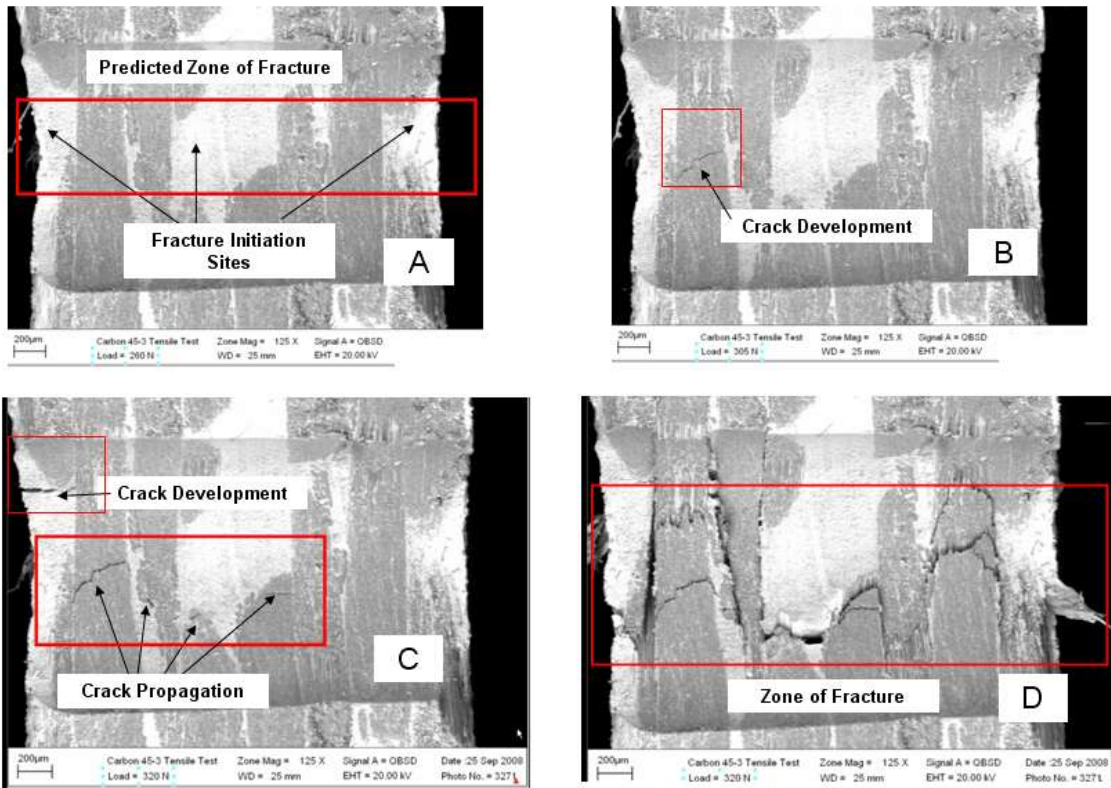


Figure 3.12: Damage evolution of carbon fiber/vinyl ester tensile sample under tensile loading.

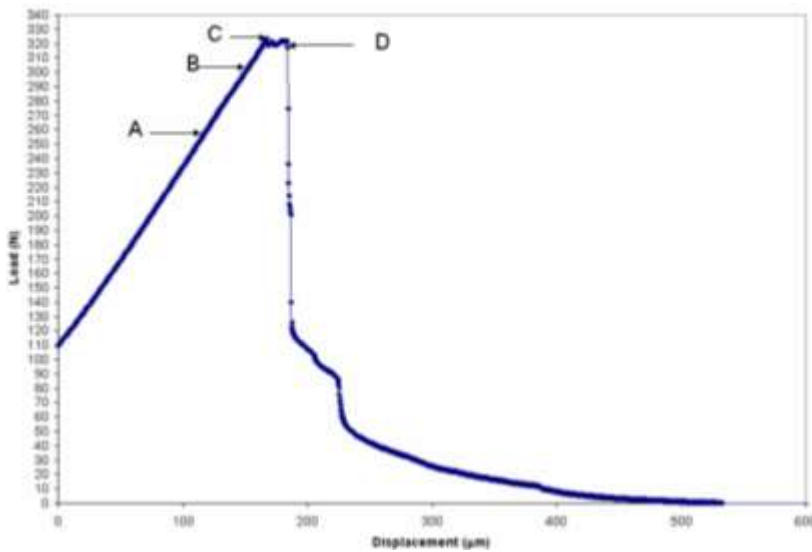


Figure 3.13 Load-Displacement damage evolution of carbon fiber/vinyl ester tensile sample under tensile loading.

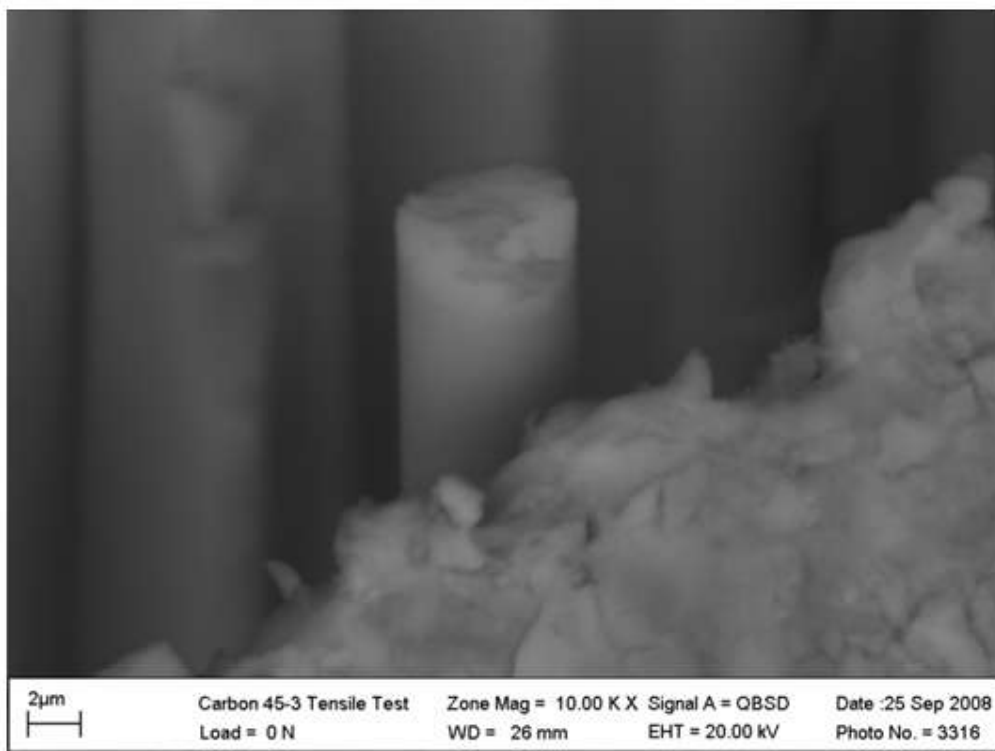
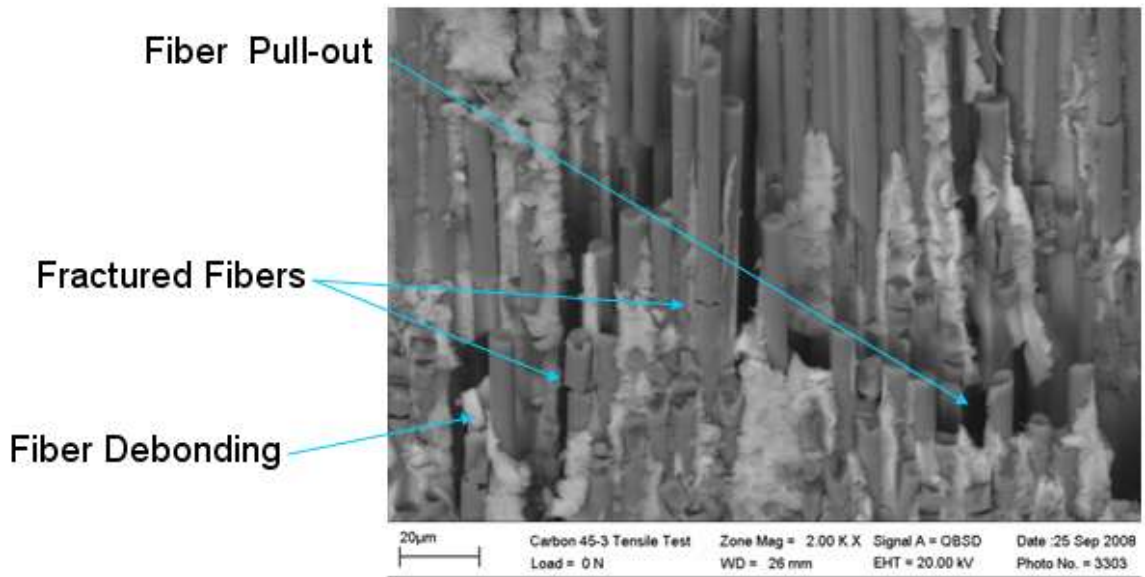


Figure 3.14: (a) Damage pattern of carbon fiber vinyl ester and (b) fracture surface of carbon fiber/vinyl ester fiber after tensile failure.

Table 3.1: Experimental Tensile Data

<b>Sample</b>	<b>Gage Length (mm)</b>	<b>Gage Area (mm<sup>2</sup>)</b>	<b>Modulus (Gpa)</b>	<b>Yield Stress (MPa)</b>	<b>Peak Stress (MPa)</b>
AF3D-1	17.78	3.28	1.84	54	64.1
AF3D-2	17.78	1.61	1.8	27.4	27.4
AF3D-3	1	1	4.2	92.7	113.8
AS3I-5	1	1	3.9	74.7	93.2
CFVE-1	1	1	4.6	112	121.3
CFVE-2	1	1	5.25	156.5	162.6
CFVE-3	1	1	5.3	129.5	129.5

## **Vita**

Stephen A. Young was born in Atlanta, Georgia on September 19, 1981. Following high school, he enrolled at University of Tennessee, Knoxville and received a Bachelor of Engineering degree in Mechanical Engineering in 2005. In 2006, Stephen started to pursue a M.S. degree in Engineering Science at University of Tennessee under the supervision of Dr. Penumadu. He obtained his masters degree in August 2009. Upon completion of M.S. he intends to continue doctoral research at U.T., working with Dr. Penumadu.